remote sensing

MDPI

Article

The Use of Superspheroids as Surrogates for Modeling Electromagnetic Wave Scattering by Ice Crystals

Lan-Hui Sun [1], Lei Bi [1,*] and Bingqi Yi [2,3]

[1] Key Laboratory of Geoscience Big Data and Deep Resource of Zhejiang Province, School of Earth Sciences, Zhejiang University, Hangzhou 310027, China; sunlh@zju.edu.cn
[2] Guangdong Province Key Laboratory for Climate Change and Natural Disaster Studies, School of Atmospheric Sciences, Sun Yat-Sen University, Guangzhou 510275, China; yibq@mail.sysu.edu.cn
[3] Southern Marine Science and Engineering Guangdong Laboratory, Zhuhai 519000, China
* Correspondence: bilei@zju.edu.cn

Abstract: Electromagnetic wave scattering by ice particles is commonly modeled by defining representative habits, including droxtals, columns, plates, and aggregates, although actual particles in the atmosphere can be even much more complex. In this study, we examined a superspheroidal approximation method for modeling electromagnetic wave scattering by ice crystals. Superspheroid can be associated with a shape index (*SI*) defined by the particle volume and average projected area. Corresponding to realistic ice crystals, suitable superspheroid models with the same *SI* (that means, identical volume and average projected area) and aspect ratio can be identified as surrogates for optical property calculations. We systematically compared the optical properties of ice crystals and superspheroids at 33 microwave bands in the range of 3–640 GHz and at three representative visible or infrared wavelengths (0.66, 2.13, and 11 μm). It was found that the single-scattering properties of compact ice crystal habits and their superspheroidal model particles were quite close. For an aggregate with sparse distribution of elements, a superspheroid model produces relatively large errors because the aspect ratio may not be sufficient to describe a particle shape. However, the optical similarity of a superspheroid and an aggregate is still encouraging.

Keywords: ice crystals; superspheroids; light scattering

Citation: Sun, L.-H.; Bi, L.; Yi, B. The Use of Superspheroids as Surrogates for Modeling Electromagnetic Wave Scattering by Ice Crystals. *Remote Sens.* **2021**, *13*, 1733. https://doi.org/10.3390/rs13091733

Academic Editor: Anthony J. Baran

Received: 1 April 2021
Accepted: 27 April 2021
Published: 29 April 2021

1. Introduction

Cirrus clouds cover approximately 20% of the earth's surface, and their radiation characteristics depend on their microphysical properties, including the shape, refractive index, and size distribution, of ice crystal particles [1–5]. In addition to cirrus clouds, precipitation clouds or ice fogs also contain various ice crystals and snowflakes depending on the ambient temperature and moisture conditions [6,7]. Therefore, substantial research has been devoted to studying the microphysics of ice crystals and their optical properties to explore the impact of ice particles on the earth's radiation budget, weather, and climate system [8–13].

Canonical ice crystal habits include hexagonal columns, plates, and aggregates [3,14]. However, ice crystals in the atmosphere can be much more complicated than canonical models [8,15–17]. Moreover, ice crystals have a wide range of particle sizes from a few microns to thousands of microns. Because of the diverse particle shapes and a wide range of particle sizes, it has been a great challenge to accurately compute the optical properties of ice particles for radiative transfer simulations, data assimilation, and remote sensing applications.

Early attempts at modeling electromagnetic wave scattering by ice crystals were based on an assumption of spherical particle shapes [1,12], followed by nonspherical approximations including simple geometries, such as spheroids and cylinders [18–22]. These explorations were greatly motivated by the robustness of the Lorenz–Mie theory [23]

and the extended boundary condition method [24,25], along with partial motivation by possible optical similarities between model particles and realistic ice crystal habits. For example, Lee et al. [26] proposed a method to simulate the light scattering characteristics of ice crystals using a circular cylinder, considering that the sharp edges of hexagonal ice particles may not be a decisive factor in light scattering calculation in the near-infrared range. The results showed that hexagonal ice particles and circular cylinders have optical similarity in the near-infrared band. Mishchenko and Macke [27] exploited the optical similarity between hexagonal column and circular cylinder to determine how big the particle size should be to have 46° halo.

However, these approximations have gradually disappeared because of the drawback of shape approximations being hard to evaluate, and a variety of computational methods have been developed that can deal efficiently with more realistic ice crystal habits. For small to moderate sizes of ice particles, numerous numerically exact methods have been developed, including the discrete dipole approximation [28,29], the finite-difference time-domain method [30,31], the pseudo-spectral time-domain method [32,33], the boundary element method [34], and the invariant imbedding T-matrix method (IITM) [35–38]. For large ice crystals, the geometric optics or physical optics methods are now common choices in research [39–46].

A few databases of the optical properties of ice crystals have been made available using the abovementioned computational methods. For example, Hess [47] used hexagonal plates and columns to establish a database of optical properties of ice crystals, including phase functions, extinction cross sections, single-scattering albedos, and asymmetry factors. Yang et al. [14] developed a comprehensive database of scattering and absorption characteristics of ice crystals in the spectrum range of 0.2–100 μm, and 11 randomly oriented ice crystal habits with maximum dimensions of 2–10,000 μm were considered. Bi and Yang [48] further improved the accuracy of this database. Hong [49] evaluated the scattering and absorption characteristics of nonspherical ice crystals in ice clouds using the discrete dipole approximation method in the microwave band of 89–340 GHz. It was found that the single-scattering characteristics of ice crystals were sensitive to their shapes. Kim [50] reported single-scattering properties of randomly oriented snow particles at microwave frequencies. Liu [51] established the single-scattering characteristics of 11 ice crystals with different shapes at 15–340 GHz. Ding et al. [52] developed a database of 12 kinds of scattering characteristics of ice crystals in the microwave spectral region and compared the conditions at 160, 200, 230, and 270 K. It was confirmed that the single-scattering characteristics of ice crystals in the microwave range depend on the temperature. More recently, Eriksson et al. [53] developed a single-scattering property database at microwave and submillimeter wavelengths with 34 ice habits. It is expected that more precise results of ice crystal properties can be obtained using more accurate ice crystal shape characterizations, although trial and tuning are needed in most applications.

This paper presents a new approach to modelling electromagnetic scattering by ice crystals. Specifically, we explore the use of superspheroids as surrogates of realistic ice habits for computing optical properties, including the extinction efficiency, single-scattering albedo, and scattering matrix. The present approach is similar to earlier optical modeling methods, such as spherical, spheroidal, and cylindrical approximations. However, superspheroids have one more degree of freedom than spheroids, which has been found to be useful and convenient for parameterizing the optical properties of nonspherical aerosol particles [54–57], even though the geometry of superspheroids can be quite different from realistic particle shapes. Physically, superspheroids can be understood as simplified models that capture optically important parameters of ice crystals (the volume, area, and aspect ratio) for optical modeling. The present research is also influenced by previous studies in the use of irregular particle models (e.g., Voronoi particles [58,59] and Gaussian random spheres [60]) to represent realistic ice crystals.

Since comprehensive light-scattering databases are available from the ultraviolet to microwave bands, a question naturally arises as to whether it is still necessary to study

superspheroidal approximation. As a matter of fact, databases only include a set of well-defined ice crystal geometries. Realistic ice particles can be much more complex, and it is challenging to manage databases with increasing number of ice crystal habits. This may also induce additional difficulty in habit selection for specific applications. In the case of ice crystals, the advantage of superspheroids is that the variation of particle shape is continuous. The model may be useful in estimating random errors associated with particle complexities and offer a complementary choice for optical modeling of ice crystals.

In view of this, this paper proposes identifying suitable superspheroidal models as surrogates of well-defined ice crystal models for computing their optical properties. We only considered randomly oriented particles in this study. The modeling capability was tested and evaluated by comparing the extinction efficiency factor, scattering efficiency factor, and scattering matrix against available databases. In particular, we highlight a new definition of the shape index (*SI*) that is valuable for finding an appropriate superspheroid with close optical similarity to a predefined ice crystal.

The remainder of this paper is organized as follows. Section 2 discusses the superspheroidal model and definition of related parameters. Sections 3 and 4 compare the computational results of superspheroids and ice crystals. The comparisons were systematically carried out in the microwave band and at a few visible and infrared wavelengths. A discussion is given in Section 5, and Section 6 concludes this study.

2. Methods and Definitions

2.1. Superspheroidal Models and Shape Index

The superspheroidal equation is defined as follows [61,62]:

$$\left(\frac{x}{a}\right)^{\frac{2}{n}} + \left(\frac{y}{b}\right)^{\frac{2}{n}} + \left(\frac{z}{c}\right)^{\frac{2}{n}} = 1, \tag{1}$$

where a, b, and c are semiaxes aligned with the x, y, and z directions in the Cartesian coordinate system, respectively, and n is referred to as the roundness parameter. Following previous studies for modeling the optical properties of dust and sea salt aerosols [55,56], we mainly studied the superspheroidal particles by assuming $a = b$. The particle shape can be changed by controlling the two parameters of aspect ratio (ξ) and roundness parameter (n). The aspect ratio (ξ) is defined as follows:

$$\xi = \begin{cases} a/c, & n > 1 \\ 2^{\frac{1-n}{2}} \cdot a/c, & n \leq 1 \end{cases}. \tag{2}$$

For the roundness parameter $n < 1$, a factor $2^{(1-n)/2}$ is introduced because the largest horizontal dimension is larger than a.

From a physical perspective of electromagnetic wave scattering by particles, the particle can be thought of as being composed of a number of electrical dipoles [23]. The total number of dipoles is determined by the wavelength and the particle volume, and the spatial distribution of dipoles is characterized by the particle shape. As the particle size increases, the extinction cross sections are fundamentally determined by the average projected area [23], which also affects the Fraunhofer diffraction. Therefore, microphysical properties, such as the aspect ratio (as a quantity to characterize the dipole distribution), volume, and average projected area of particles, have an important impact on the optical properties of particles. Thus, to identify a surrogate for a given ice crystal particle, the most suitable candidate is the superspheroid that has the same aspect ratio, volume, and projected area as the ice crystal. For this purpose, a shape index *SI* is defined as follows:

$$SI = \frac{3V}{4\pi(S/\pi)^{3/2}}, \tag{3}$$

where V is the volume and S is the average projected area of the particle. According to Equation (3), if SI is the same for two different particles, then their volume and average projected area are identical.

Figure 1 shows the variation of SI with respect to the aspect ratio and the roundness of particles. The SI of spherical particles is 1 and that of superspheroidal particles is less than 1. In addition, for the same SI, superspheroidal models also allow additional freedom to change the aspect ratio. Therefore, with a predefined ice crystal model, by defining SI, superspheroidal models can be changed to approach the aspect ratio, volume, and average projected area of ice crystal particles concurrently. Figure 2 shows representative ice crystals and their superspheroidal counterparts. For the shapes of droxtal, 8-column aggregate, 5-plate aggregate, and 10-plate aggregate with the same aspect ratio and SI parameters, the superspheroids simulated the ice crystals. For the column and plate, their shapes changed with the size of the particles, so the superspheroids corresponding to three ice crystal particles with different sizes are listed here. The SIs of ice crystals and the aspect ratios and roundness parameters of superspheroid counterparts are given in Table 1.

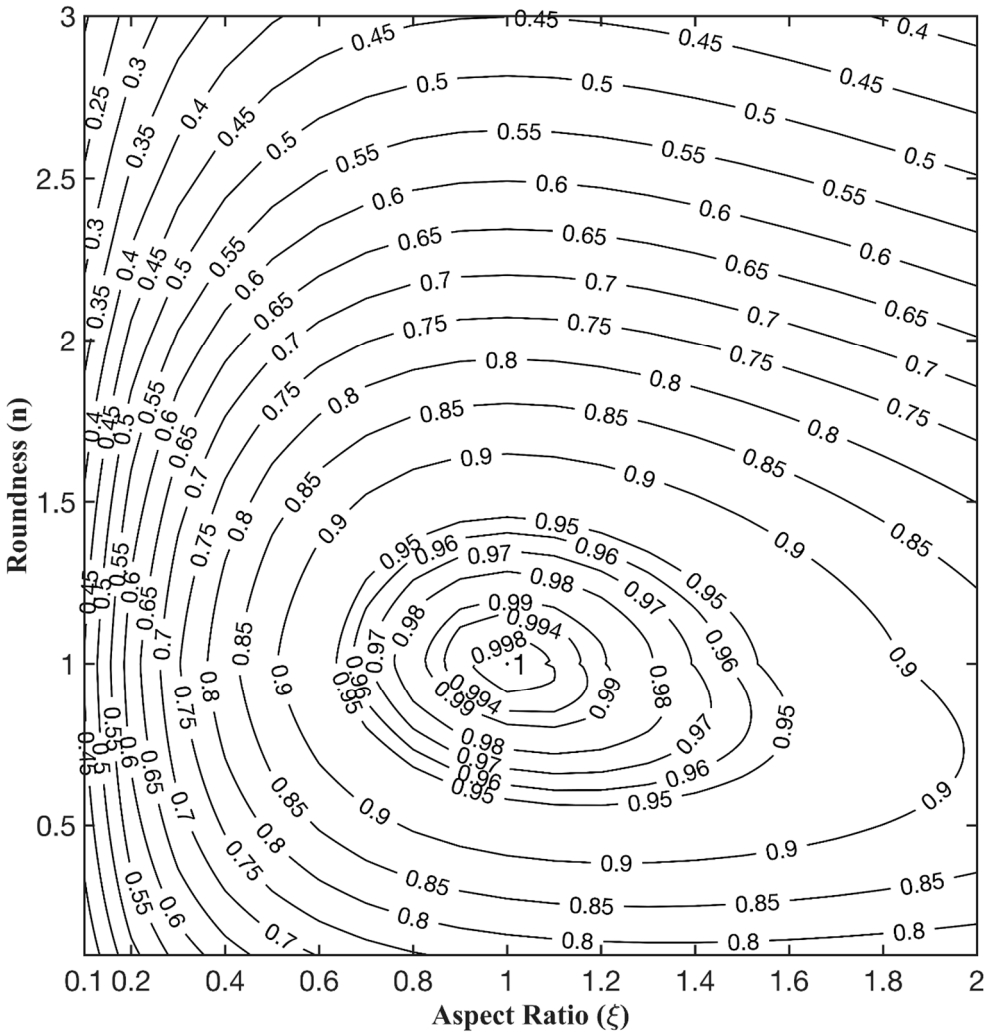

Figure 1. Shape index (SI) in a two-dimensional space constructed by aspect ratio (ξ) and roundness parameter (n).

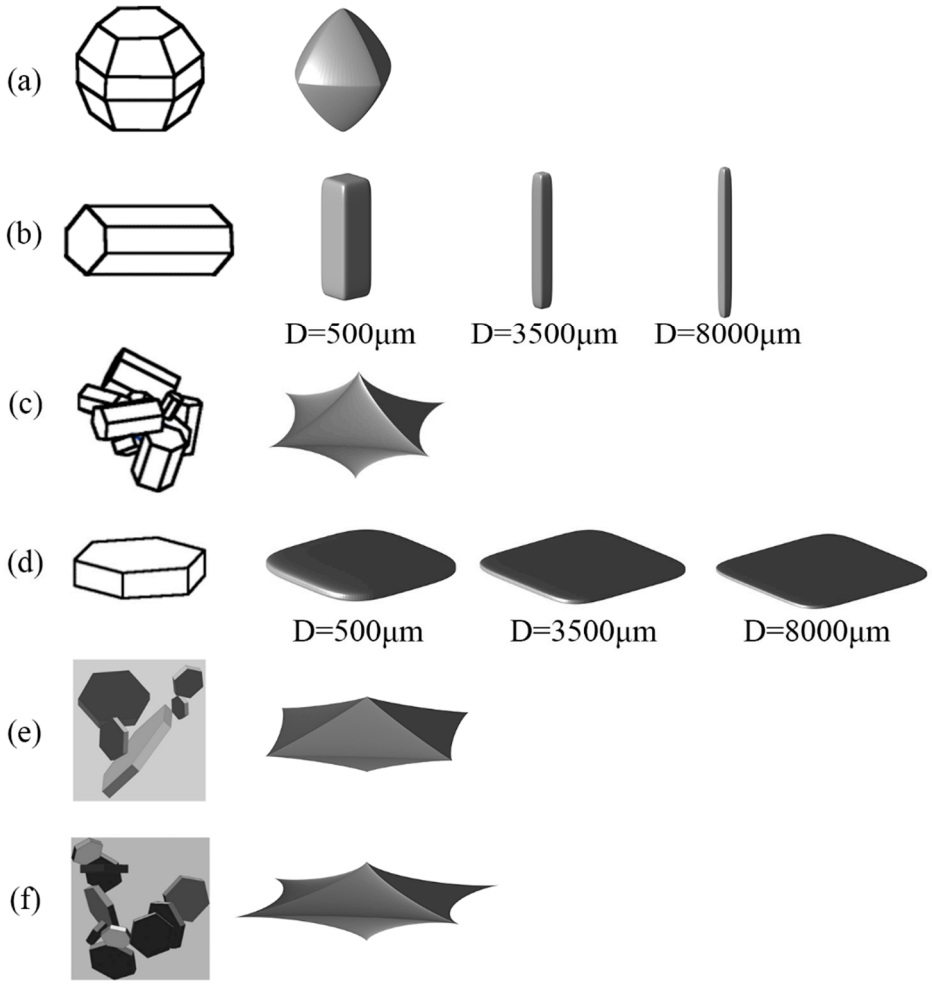

Figure 2. Ice crystal models and their superspheroidal counterparts. Droxtal (**a**), 8-column (**c**), 5-plate (**e**), and 10-plate (**f**) aggregates are simulated by superspheroids of a single shape. The shape of superspheroids corresponding to column (**b**) and plate (**d**) changes with the particle size D. D is defined as the maximum dimension and can be found in Yang et al. [14]. Here, D is taken as 500, 3500, and 8000 μm for example.

Table 1. The aspect ratio (ξ), roundness parameter (n), and shape index (SI) for superspheroid surrogates. For the column and plate, SIs are different for different sizes.

Ice Habits		Superspheroid Model	*SI*
droxtal		ξ = 0.889, n = 1.6	0.9114
column	D = 500 μm	ξ = 0.31, n = 0.21	0.6135
	D = 3500 μm	ξ = 0.12, n = 0.29	0.1176
	D = 8000 μm	ξ = 0.08, n = 0.33	0.3528
plate	D = 500 μm	ξ = 14.67, n = 0.79	0.2554
	D = 3500 μm	ξ = 40.83, n = 0.35	0.1052
	D = 8000 μm	ξ = 60.07, n = 0.32	0.0701
8-column aggregate		ξ = 2, n = 2.7	0.4468
5-plate aggregate		ξ = 3.4, n = 2.2	0.4202
10-plate aggregate		ξ = 4, n = 2.7	0.2269

2.2. Optical Properties

Ice clouds in the atmosphere present as an ensemble of ice crystals of different sizes. Therefore, it is necessary to compute the bulk scattering characteristics of ice crystals per

unit volume. The scattering coefficient b_{sca} and extinction coefficient b_{ext} are given as follows [23]:

$$b_{sca} = \int_{D_1}^{D_2} C_{sca}(D)n(D)dD = \int_{D_1}^{D_2} S(D)Q_{sca}(D)n(D)dD, \quad (4)$$

$$b_{ext} = \int_{D_1}^{D_2} C_{ext}(D)n(D)dD = \int_{D_1}^{D_2} S(D)Q_{ext}(D)n(D)dD, \quad (5)$$

where C_{sca} is the scattering cross section, which is the product of the average projected area S and the scattering efficiency factor Q_{sca}. C_{ext} and Q_{ext} are the extinction cross section and the extinction efficiency factor, respectively. D is the maximum dimension of ice crystals, and the size distribution $n(D)dD$ represents the particle number concentration within (D, D+dD) per volume. In computations, D_1 = 2 μm and D_2 = 10,000 μm. For randomly oriented superspheroids, the relationship between the Stokes vectors of an incident wave $[I,\ Q,\ U, V]_{inc}$ and a scattering wave $[I,\ Q,\ U,\ V]_{sca}$ is given by the scattering matrix [23]:

$$\begin{bmatrix} I(\theta) \\ Q(\theta) \\ U(\theta) \\ V(\theta) \end{bmatrix}_{sca} \propto \begin{bmatrix} P_{11}(\theta) & P_{12}(\theta) & 0 & 0 \\ P_{12}(\theta) & P_{22}(\theta) & 0 & 0 \\ 0 & 0 & P_{33}(\theta) & P_{34}(\theta) \\ 0 & 0 & -P_{34}(\theta) & P_{44}(\theta) \end{bmatrix} \begin{bmatrix} I(\theta) \\ Q(\theta) \\ U(\theta) \\ V(\theta) \end{bmatrix}_{inc}, \quad (6)$$

where θ is the scattering angle in the range of 0 to 180°. Because of the symmetry of the superspheroid, eight off-diagonal elements of the scattering matrix are all 0. The incident and scattering Stokes vectors are defined relative to the scattering plane, where I is the total intensity, Q and U describe the linear polarization intensity, and V describes the circular polarization intensity. The bulk scattering matrix is given by [63]:

$$\langle P_{ij} \rangle = \frac{\int_{D_1}^{D_2} P_{ij}(D)C_{sca}(D)n(D)dD}{b_{sca}}, \quad (7)$$

where P_{ij} is an element in the scattering matrix, C_{sca} is the scattering cross section, and b_{sca} is the scattering coefficient. In this paper, we used the standard gamma distribution [63]:

$$n(D) = \frac{(D_m \cdot v_e)^{\frac{2 \cdot v_e - 1}{v_e}}}{\Gamma\left(\frac{1-2 \cdot v_e}{v_e}\right)} \cdot D^{\frac{1-3 \cdot v_e}{v_e}} \cdot e^{\frac{-D}{D_m \cdot v_e}}, \quad (8)$$

where D is the maximum dimension, D_m is the effective diameter, and v_e is the effective variance.

The superspheroidal approximation was examined by referencing the optical properties of droxtals, columns, plates, 8-column aggregates, 5-plate aggregates, and 10-plate aggregates from optical property databases [14,48,52]. The optical properties of the superspheroidal particles were computed from the IITM and the improved geometric optics method (IGOM) [44]. The applicability regimes of superspheroidal approximations can be examined by comparing the extinction efficiency, scattering efficiency, asymmetry factor, and phase matrix of well-defined ice crystal habits and their superspheroid counterparts.

3. Microwave Bands

The experimental temperature was assumed to be 160 K, and the frequency range was 3–640 GHz with 33 bands. The temperature-dependent complex refractive indices were taken from Iwabuchi and Yang [64]. For each ice crystal model, a total of 24 particle sizes in the range of 2–10,000 μm were selected. The IITM was used for all the computations in the microwave bands. The optical properties examined included the extinction efficiency factor Q_{ext}, scattering efficiency factor Q_{sca}, phase matrix element P_{ij}, and asymmetry factor g.

3.1. Superspheroids for Droxtal

According to the *SI* and the aspect ratio values of a droxtal (see Table 1), a superspheroidal model with an aspect ratio of 0.9 and roundness parameter of 1.6 was identified. We note that superspheroids with roundness parameters of 0.5 and 1.6 both satisfy the condition. The results of two superspheroids were found to be close. The roundness of 1.6 was selected because of a slightly better comparison to the results of droxtal.

Although the droxtal particle and the superspheroid particle have obviously different geometries, they have identical volume, average projected area, and aspect ratios. Figure 3 shows the simulation results of the extinction efficiency, scattering efficiency, and asymmetry factor at 33 bands in the frequency range of 3–640 GHz. The maximum dimensions were 3000 and 9000 μm (the sizes were selected for the method examination; note that realistic droxtal ice crystal may not have such large particle sizes). We found that the trends of these results were the same as those of the superspheroid, and the values were very close. Because the particle size was fixed, the size parameter increased with the frequency. Both the droxtals and superspheroids showed similar resonance effect as the size parameter varied.

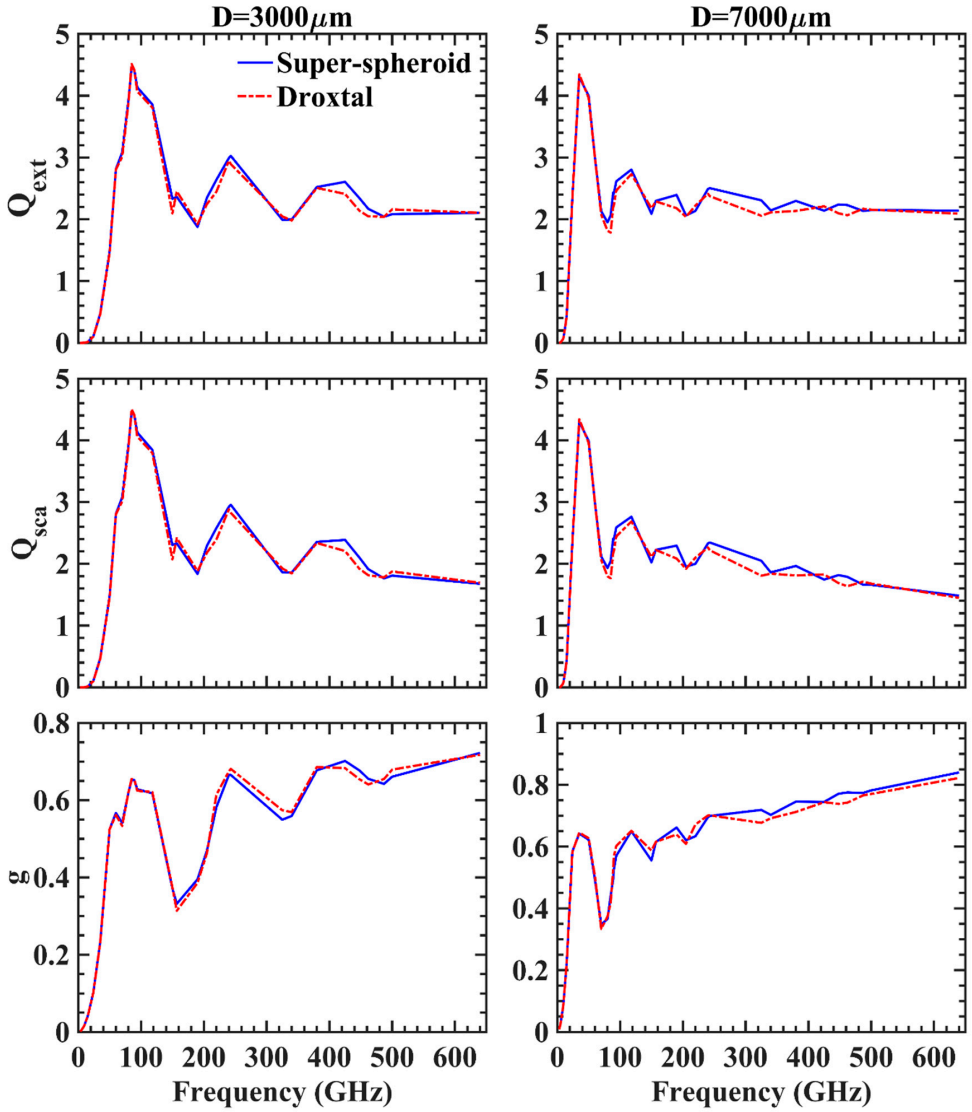

Figure 3. Comparison of the extinction efficiency, scattering efficiency, and asymmetry factor of a droxtal ice crystal and its corresponding superspheroid in the frequency range of 3–640 GHz. The maximum dimensions of the droxtal ice crystal were selected as 3000 (**left**) and 7000 (**right**) μm.

At the lower end of the frequency, the size parameter was quite small and the shape effect was negligible, so the agreement was better. With the increase of size parameters, the particle shape was expected to exert a greater influence on the optical properties of particles. However, in the comparisons, the differences between droxtal and superspheroids were small. This means that the volume, projected area, and aspect ratio are optically important parameters that determine the optical properties. Therefore, it is reasonable to use superspheroids as surrogates of droxtal ice particles.

Next, we examined the scattering matrix. Figure 4 compares six nonzero scattering-matrix elements of droxtals and superspheroids. The frequency was 220 GHz, and the maximum dimensions were 500, 4000, and 9000 μm. For the first column, where the maximum dimension was 500 μm, the nonsphericity effect was almost invisible, as shown by element P_{22}/P_{11} (=1), which is an indicator of nonsphericity. The scattering matrix elements from the two different models were almost identical and showed Rayleigh scattering behavior.

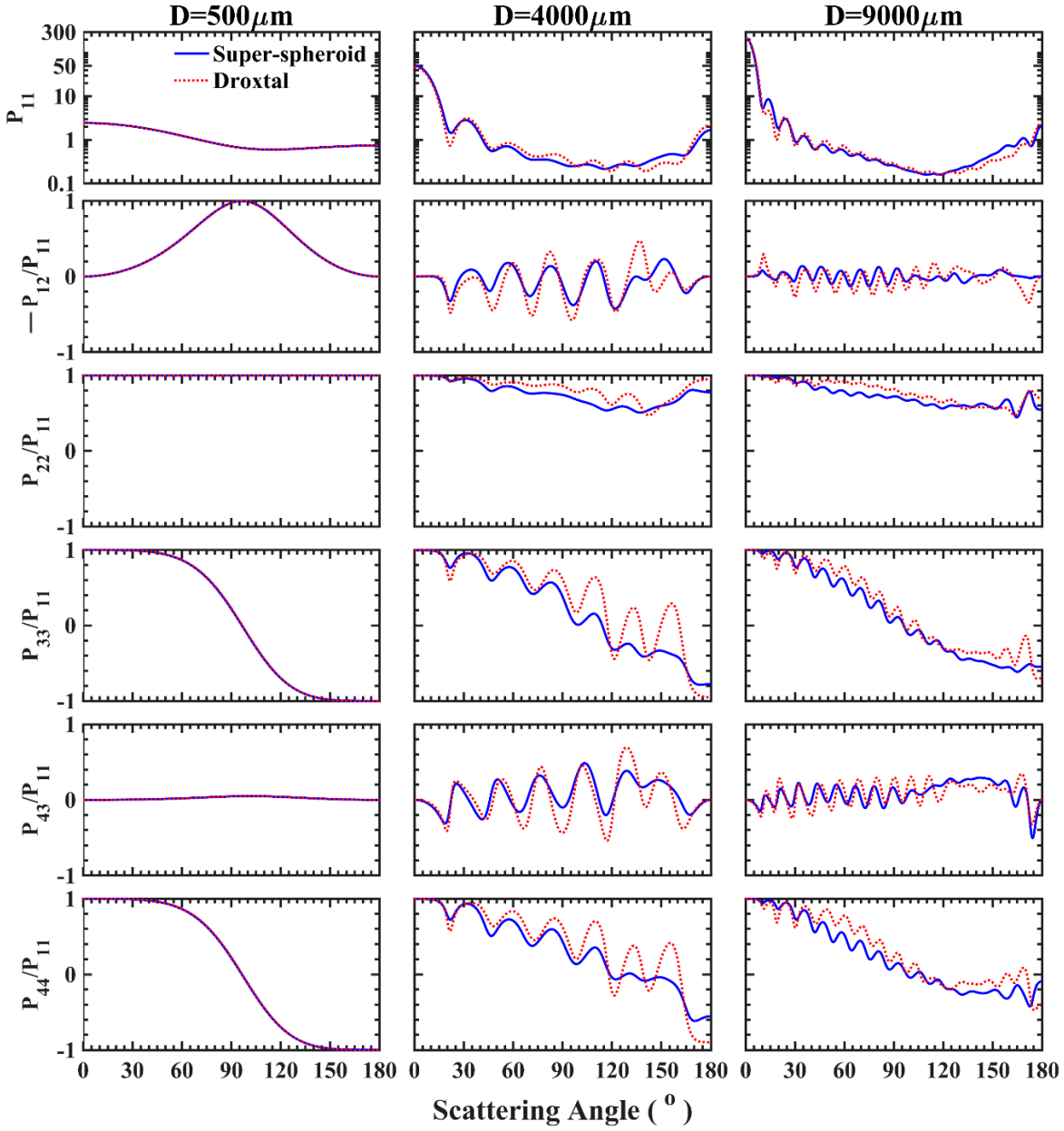

Figure 4. Scattering matrix elements for a droxtal ice crystal and its superspheroidal counterpart at the frequency of 220 GHz. The maximum dimensions of the droxtal ice crystal were selected as 500 (**left**), 4000 (**middle**), and 9000 (**right**) μm.

For the second and third columns, as the size parameter increased, all scattering matrix elements showed strong oscillations, and the influence of particle shape on the scattering characteristics became visible. The scattering matrix elements of superspheroids and droxtals showed some differences. However, the trends of the scattering matrix elements with respect to the scattering angle for the two geometries were obviously consistent. This means that the superspheroid model offers a good approximation of droxtal geometries for computing the scattering phase matrix. Note that the spherical approximation failed to produce most features (see Yang et al. [65]).

To compute the bulk scattering optical properties, a standard gamma distribution with an effective maximum dimension of 4000 μm and an effective variance of 0.1 was used to integrate the single-scattering properties. The results in the 220 GHz band are shown in Figure 5. As expected, most oscillation features in Figure 4 were cancelled out, resulting in a closer agreement between the results computed for the droxtal and superspheroid models. Note that P_{22}/P_{11} values deviated more from unity for the superspheroid than the droxtal. The scattering and extinction coefficients for the droxtal and the superspheroid were close (see Table 2).

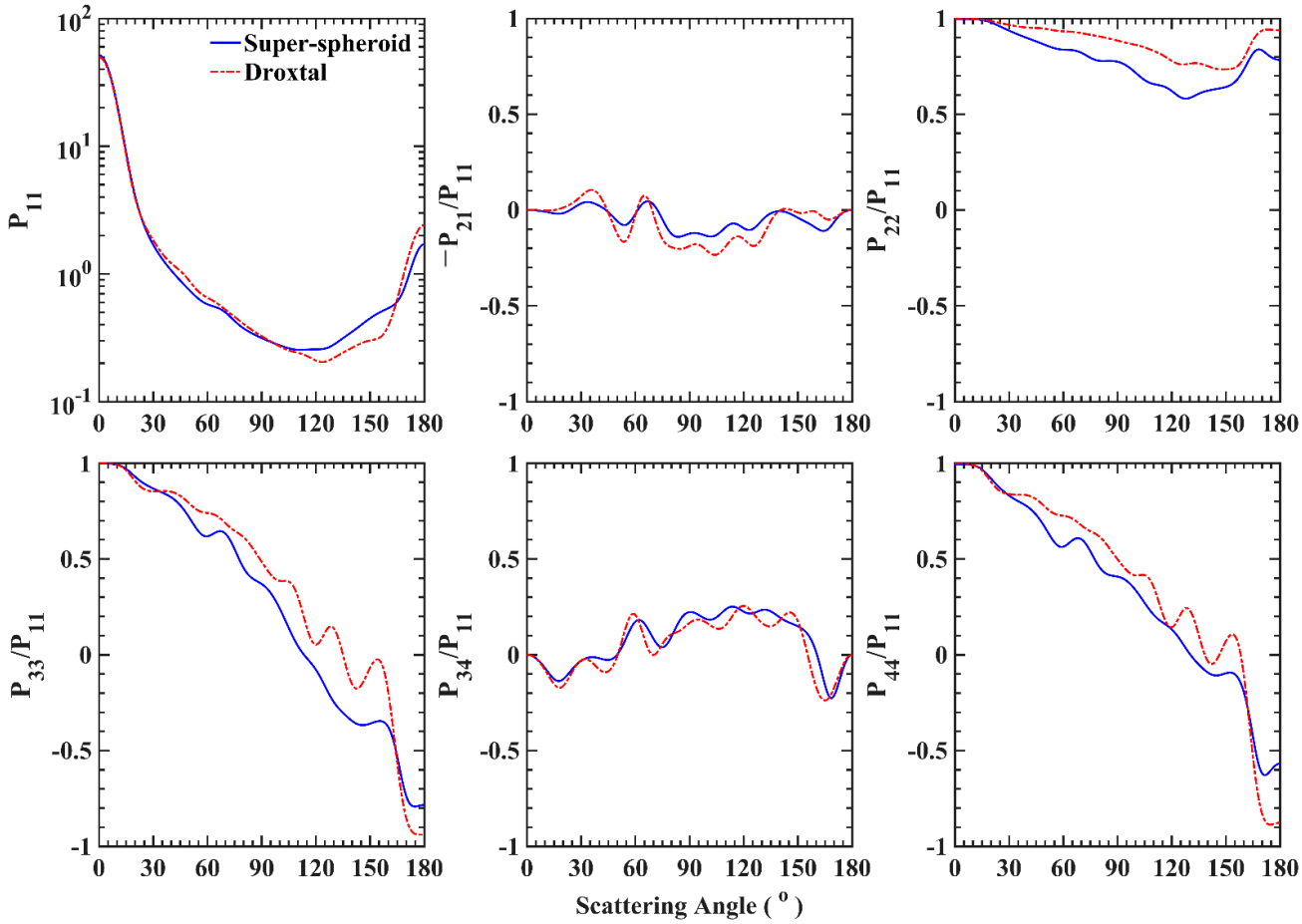

Figure 5. Bulk scattering matrix of droxtal ice crystal and its superspheroidal counterpart at the frequency of 220 GHz. The effective diameter (D_m) is 4000 μm, and the effective variance (v_e) is 0.1 in the gamma size distribution.

3.2. Superspheroids for Columns

The aspect ratio of column particles varies with the particle size. The relationship between the aspect ratio and size is given as follows [66,67]:

$$2a/L = \begin{cases} 0.7, & L < 100\ \mu\text{m} \\ 6.96/\sqrt{L}, & L \geq 100\ \mu\text{m} \end{cases}, \quad (9)$$

where a is the semiwidth, and L is the length. As such, superspheroids for different particle sizes are also different. Figure 6 shows a comparison of the extinction efficiency factor, scattering efficiency factor, and asymmetry factor computed for columns and superspheroids in the frequency range of 3–640 GHz. Maximum dimensions of 3000 and 7000 μm were chosen for comparison. Close agreement was again obtained between the results from the two different models.

Table 2. The scattering (extinction) coefficients of different ice models and their corresponding superspheroids.

Ice Habits	b_{sca} (b_{ext}) (m^{-1})	
	Realistic Model	**Superspheroid**
droxtal	18.00 (18.68)	18.43 (19.03)
column	1.50 (1.50)	1.56 (1.56)
plate	2.07 (2.08)	2.03 (2.04)
8-column aggregate	26.97 (27.41)	20.48 (20.94)
5-plate aggregate	21.26 (21.47)	15.60 (15.84)
10-plate aggregate	18.97 (19.07)	12.17 (12.31)

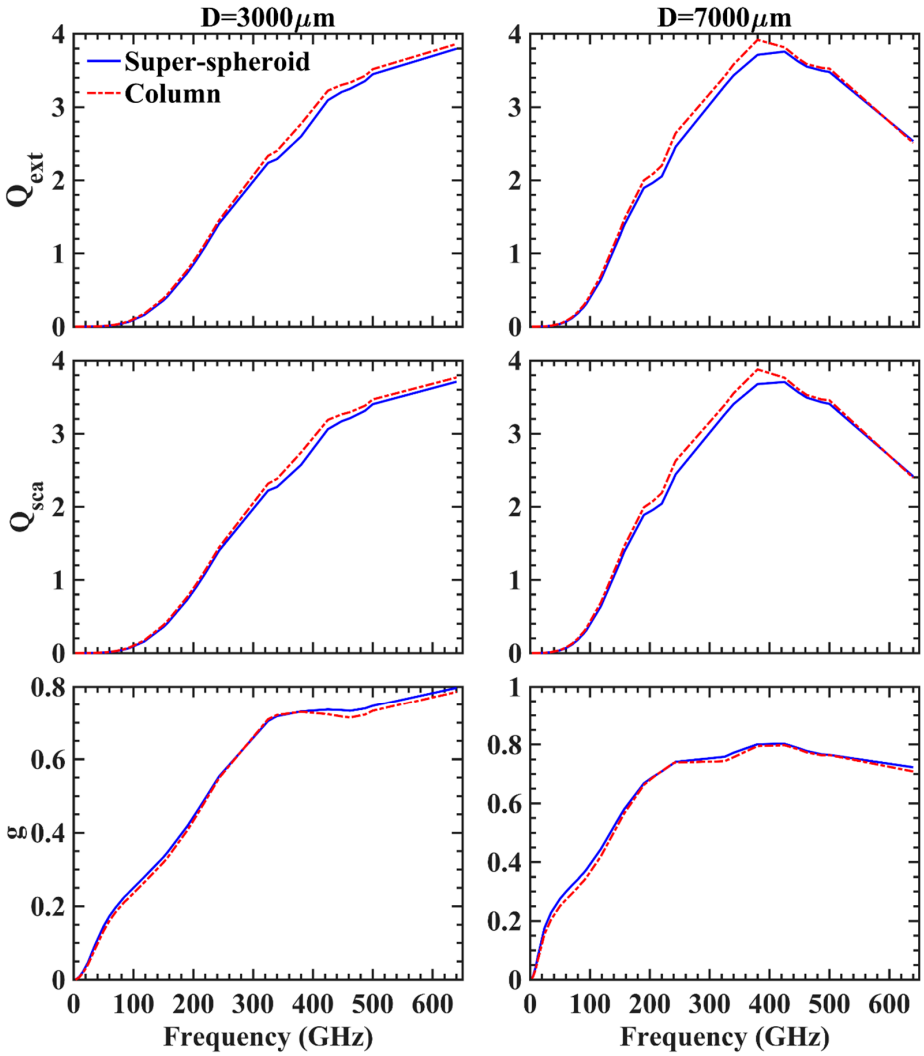

Figure 6. Comparison of the extinction efficiency, scattering efficiency, and asymmetry factor of a hexagonal column ice crystal and its corresponding superspheroid in the frequency range of 3–640 GHz. The maximum dimensions of column ice crystal were selected as 3000 (**left**) and 7000 (**right**) μm.

The scattering matrix was also compared for ice columns and superspheroids with multiple sizes, as shown in Figure 7. With the increase of particle size, the error increased gradually, but the trends were consistent. The simulation error of phase function P_{11} was visibly small for most particle sizes. Figure 8 shows the bulk scattering matrix elements at 220 GHz. Similar to the droxtal case, after the size integration, the differences in the scattering matrix elements were reduced to some extent, and better agreement was reached. The scattering and extinction coefficients for the column and the superspheroid were close (see Table 2).

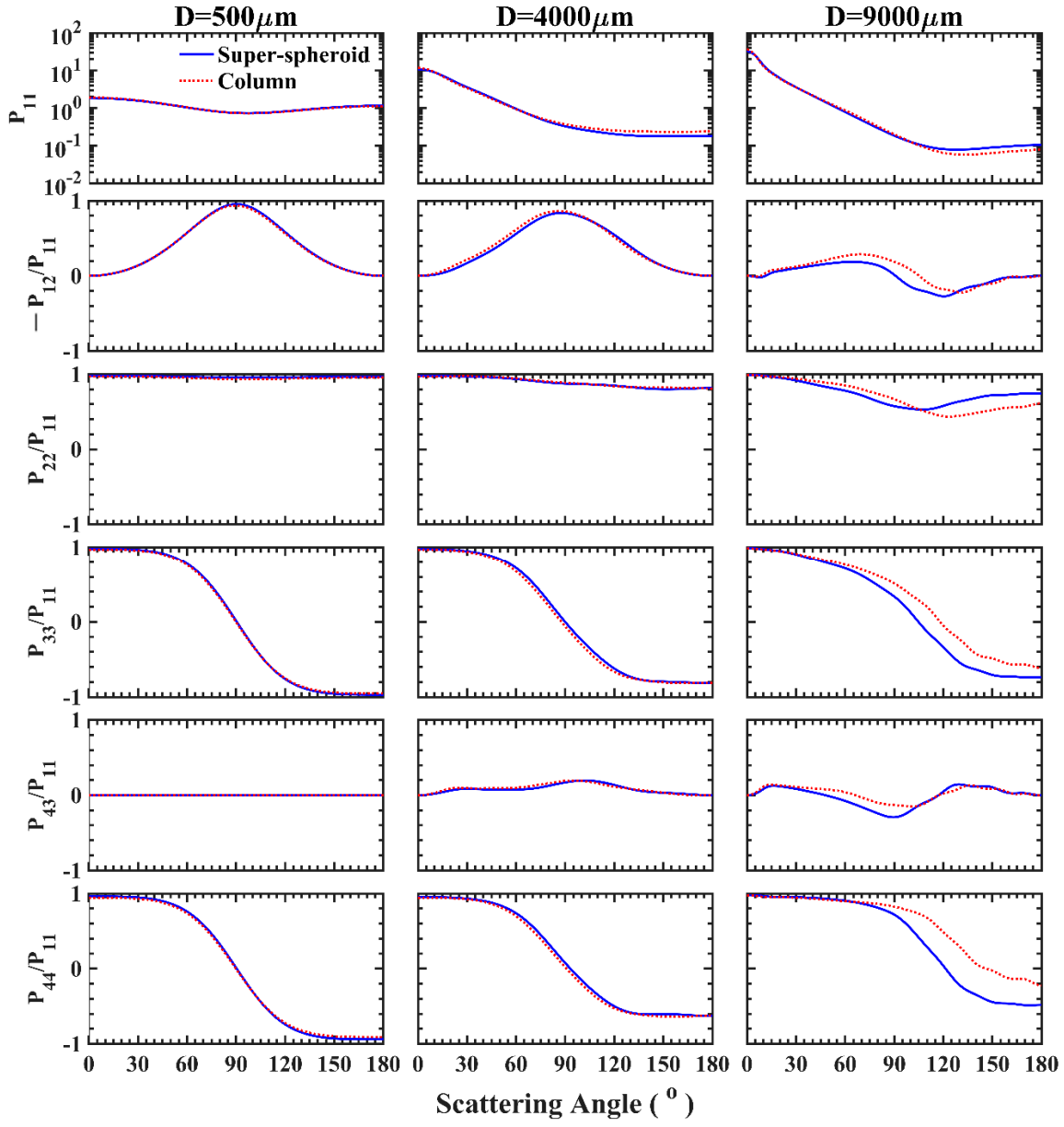

Figure 7. Scattering matrix elements for hexagonal columns and their superspheroidal counterparts at the frequency of 220 GHz. The maximum dimensions of column ice crystal were selected as 500 (**left**), 4000 (**middle**), and 9000 (**right**) μm.

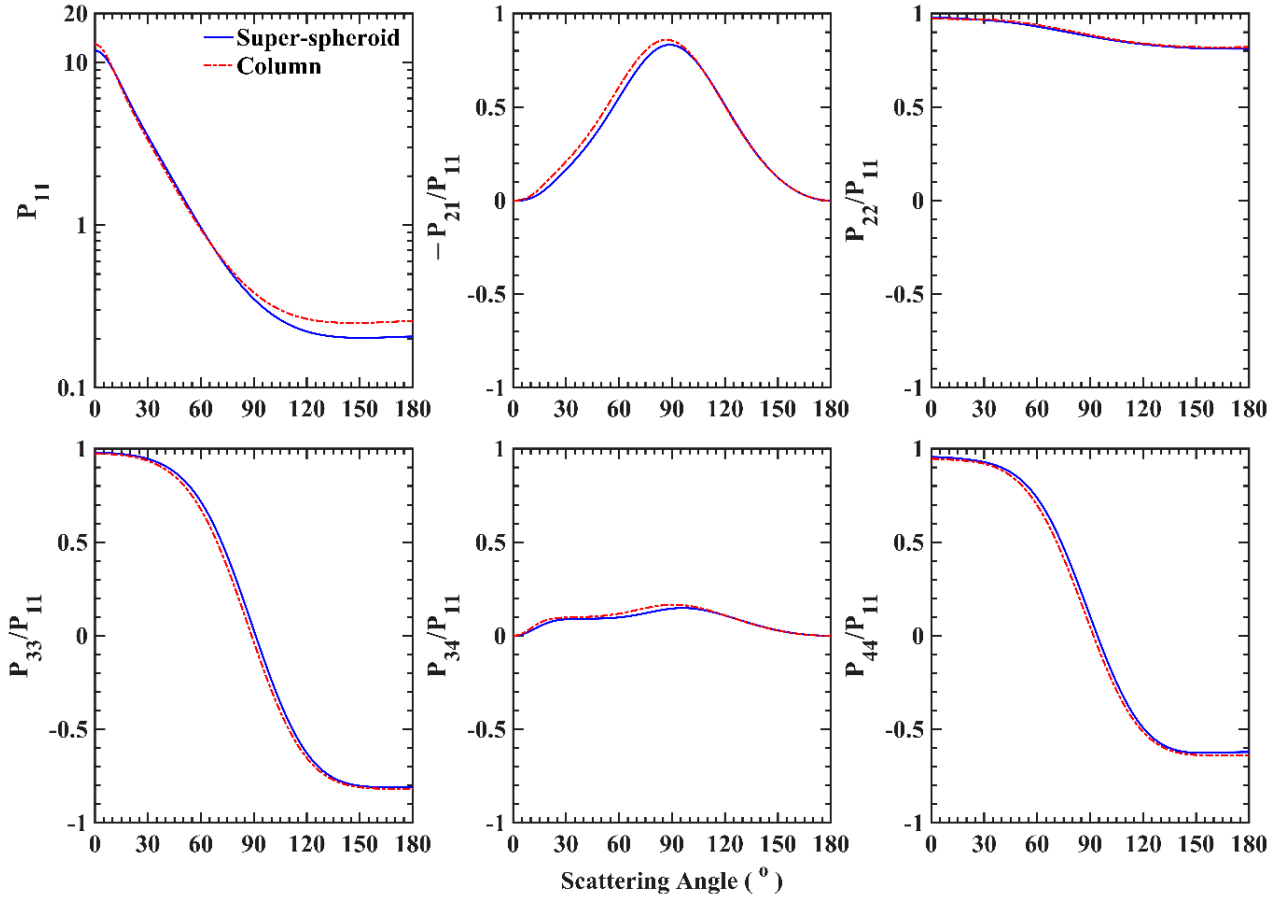

Figure 8. Bulk scattering matrix of hexagonal column ice crystal and its superspheroidal counterpart at the frequency of 220 GHz. The effective diameter (D_m) is 4000 μm, and the effective variance (v_e) is 0.1 in the gamma size distribution.

3.3. Superspheroids for Plates

The relationship between the aspect ratio of a plate and its maximum dimension is given as follows [68]:

$$2a/L = \begin{cases} 1, & a \le 2\ \mu\text{m} \\ 0.2914 \cdot a + 0.4172, & 2 < a < 5\ \mu\text{m}, \\ 0.8038 \cdot a^{0.526}, & a \ge 5\ \mu\text{m} \end{cases} \quad (10)$$

Figure 9 compares the efficiency factors and asymmetry factor of superspheroids and plates with different sizes at 3–640 GHz. As can be seen, for D of 3000 μm, the efficiency factor of superspheroids was a little bit smaller in the frequency band of 500–640 GHz, and the asymmetry factor was slightly larger in the frequency band of 3–100 GHz. For D of 7000 μm, the efficiency factor of the superspheroids was lower at 300–400 GHz, but the asymmetry factor was fairly close. In general, the two results showed good agreement. Figure 10 compares the results of scattering matrix elements for small, medium, and large sizes in the 220 GHz band. It was found that the simulation of P_{11} and the other elements from superspheroidal models also fit the ice plate results well. Taking D_m = 4000 μm and v_e = 0.1 as an example, the bulk scattering results at 220 GHz are shown in Figure 11. The scattering and extinction coefficients for the plate and superspheroid are given in Table 2.

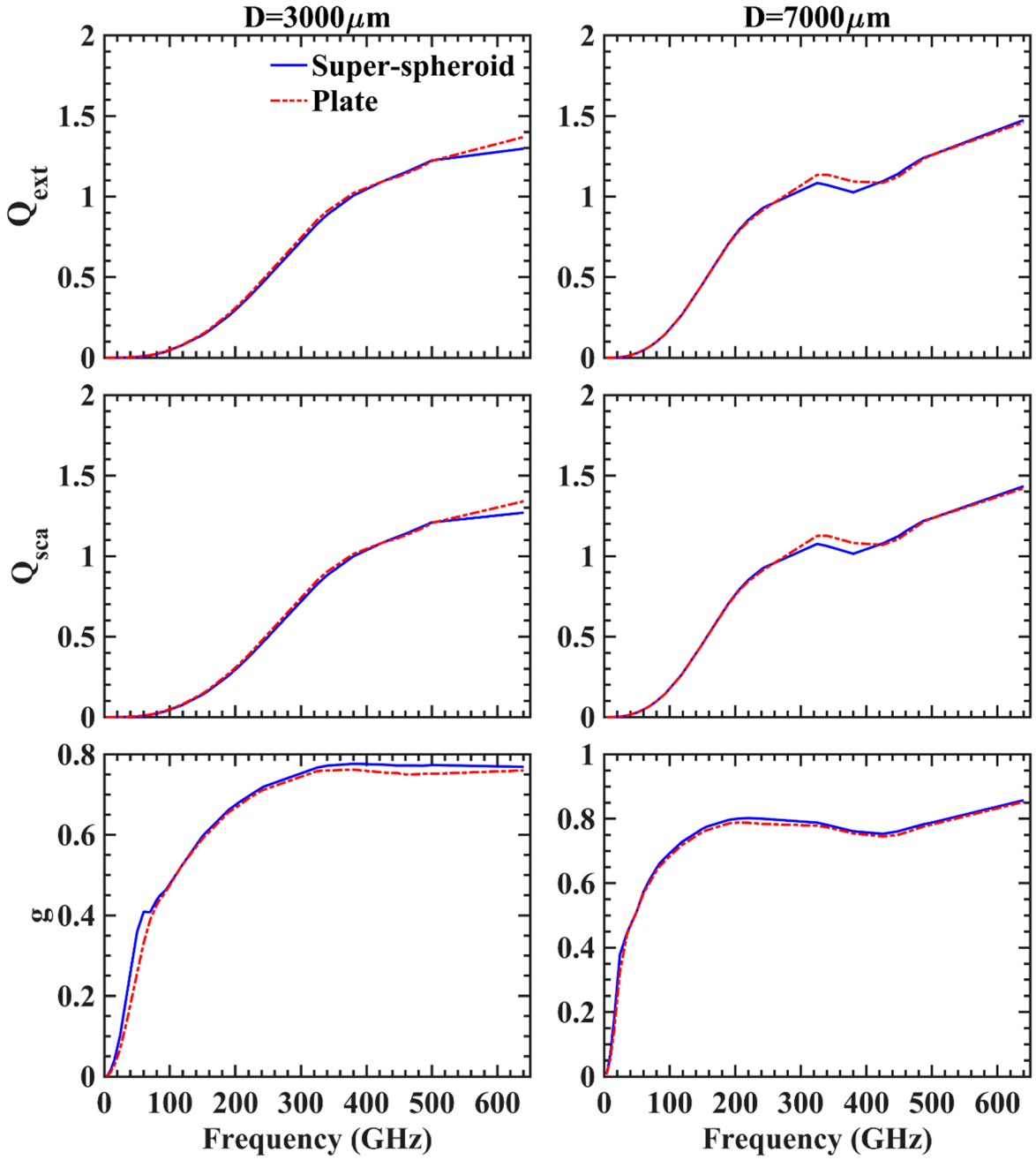

Figure 9. Comparison of the extinction efficiency, scattering efficiency, and asymmetry factor of hexagonal plate ice crystals and their corresponding superspheroids in the frequency range of 3–640 GHz. The maximum dimensions of plate ice crystal were selected as 3000 (**left**) and 7000 (**right**) μm.

3.4. Superspheroids for an 8-Column Aggregate

The 8-column aggregate is a more complex particle shape than droxtals and hexagonal columns/plates. It is currently used as the ice crystal model in the Moderate Resolution Imaging Spectroradiometer (MODIS) Collection 6 product [69]. Considering the aspect ratio, average projected area, and volume, the selected superspheroid model had an aspect ratio of 2 and a roundness parameter of 2.7. The scattering characteristics of superspheroids and the 8-column aggregate at each frequency band were compared.

Figure 12 compares the extinction, scattering, and asymmetry factor of the aggregate and a single superspheroid. In contrast to the previous comparisons, the differences were relatively large. The fundamental reason may be that the aspect ratio is not sufficient to

describe the particle shape. The mutual interactions between particle elements may also be important. However, from comparison of the scattering matrix elements (Figure 13), the optical similarity is still encouraging. Figure 14 shows the bulk scattering characteristics of the superspheroids and the aggregate particle at 220 GHz. In this figure, D_m is 7000 μm and v_e is 0.1. It can be seen that the overall trend of the two results was consistent, and the error was smaller. The scattering and extinction coefficients for the 8-column aggregate and the superspheroid counterpart are given in Table 2.

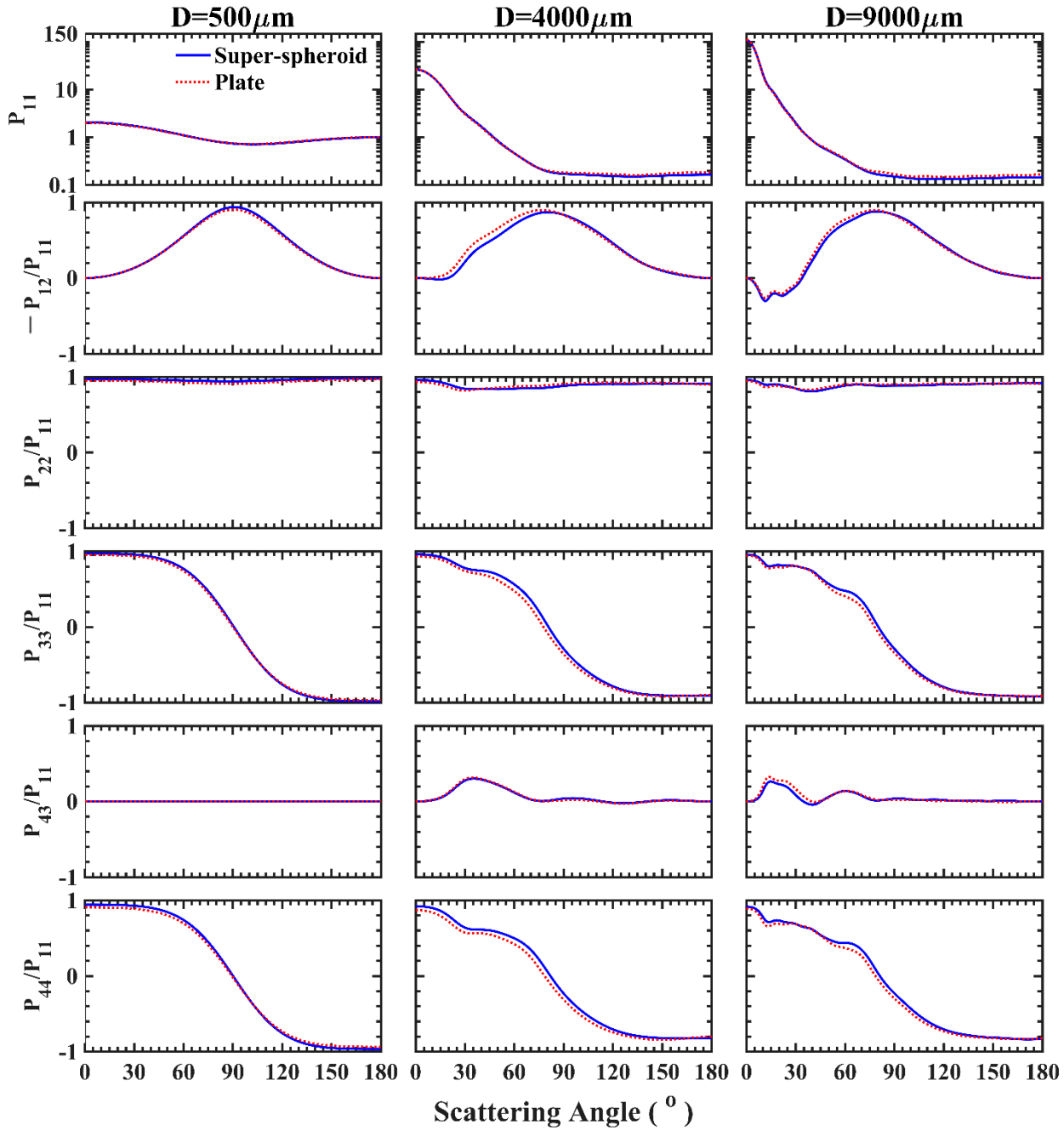

Figure 10. Scattering matrix elements for plate and superspheroids at the frequency of 220 GHz with the maximum dimensions of 500 (**left**), 4000 (**middle**), and 9000 (**right**) μm.

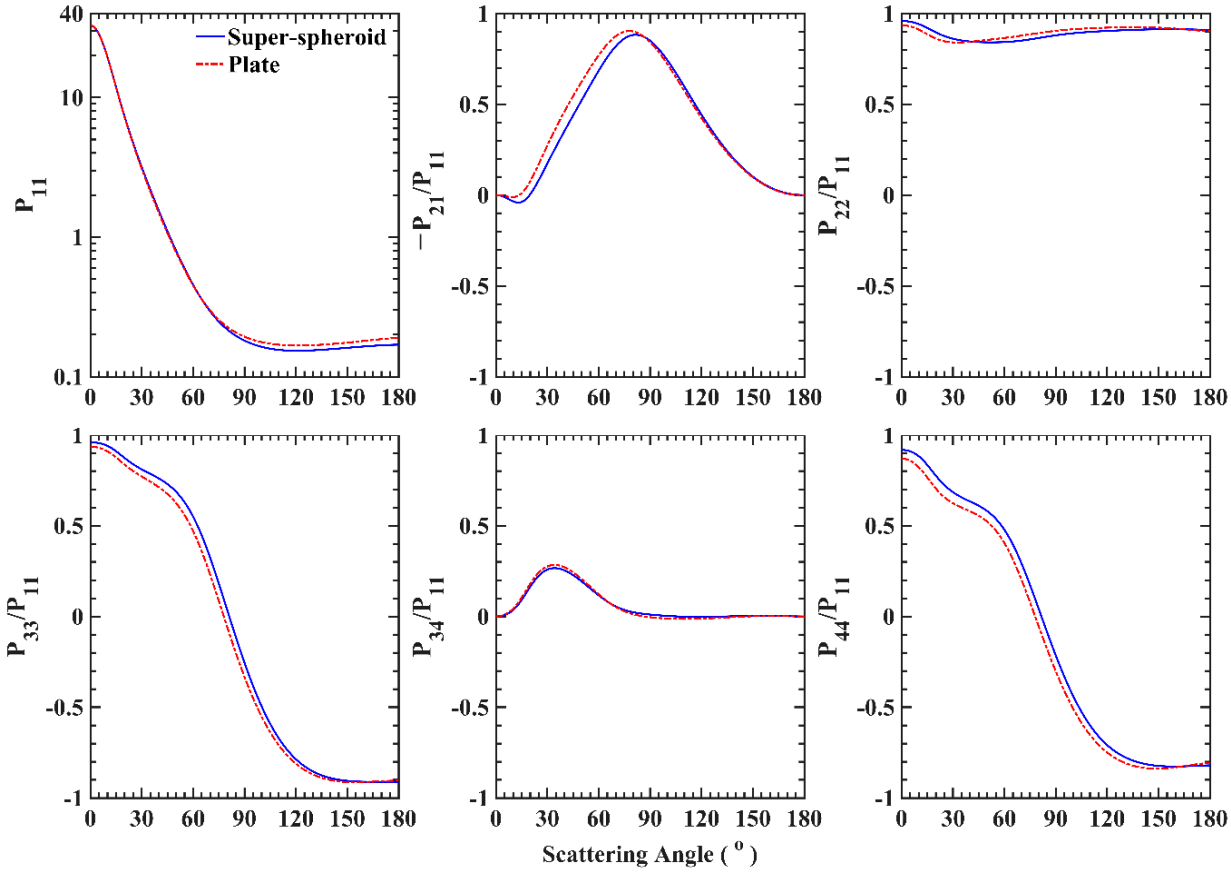

Figure 11. Bulk scattering matrix for plates and superspheroids at 220 GHz. The effective diameter (D_m) is 4000 μm, and the effective variance (v_e) is 0.1.

3.5. Superspheroids for Sparse Aggregate Shapes: 5-Plate and 10-Plate Aggregates

The optical properties of 5-plate and 10-plate aggregates are shown in Figure 15. Different from the 8-column aggregate, the two plate aggregates were sparsely distributed. According to Fox [70], the mass–dimension relationship of the 8-column aggregate is quite different from other models and observations, which emphasizes the necessity of studying sparse ice aggregates for optical simulations because their mass–dimension relationship could be more reasonable. The optical similarities of these sparse shapes and their superspheroidal counterparts might not be as good as those of compact ice crystals because the use of the aspect ratio to describe the particle shape could be oversimplified. Although each element can be modeled as a superspheroid, the aggregation process could complicate the calculation of optical properties, which is against the original motivation of using a simple modeling approach.

According to the *SI* and the aspect ratio of the 5-plate aggregate, a superspheroid model with an aspect ratio of 3.4 and roundness of 2.2 was selected. For the 10-plate aggregate, the superspheroid model's aspect ratio was 4.0, and the roundness was 2.7. Figure 15 compares *Qsca*, *Qext*, and *g* between the superspheroids and the two aggregate models in 33 bands from 3 to 640 GHz. The extinction and scattering coefficients for the two different shapes had large differences, particularly for larger frequencies. However, the asymmetry parameters of the aggregates and their superspheroidal counterparts were close. Similar to the 8-column aggregate case, the scattering matrix elements of the superspheroid model and the plate aggregates resembled each other (see Figure 16). The phase function P_{11} of the superspheroid was smoother than that of the ice crystal model, and the backward scattering was lower.

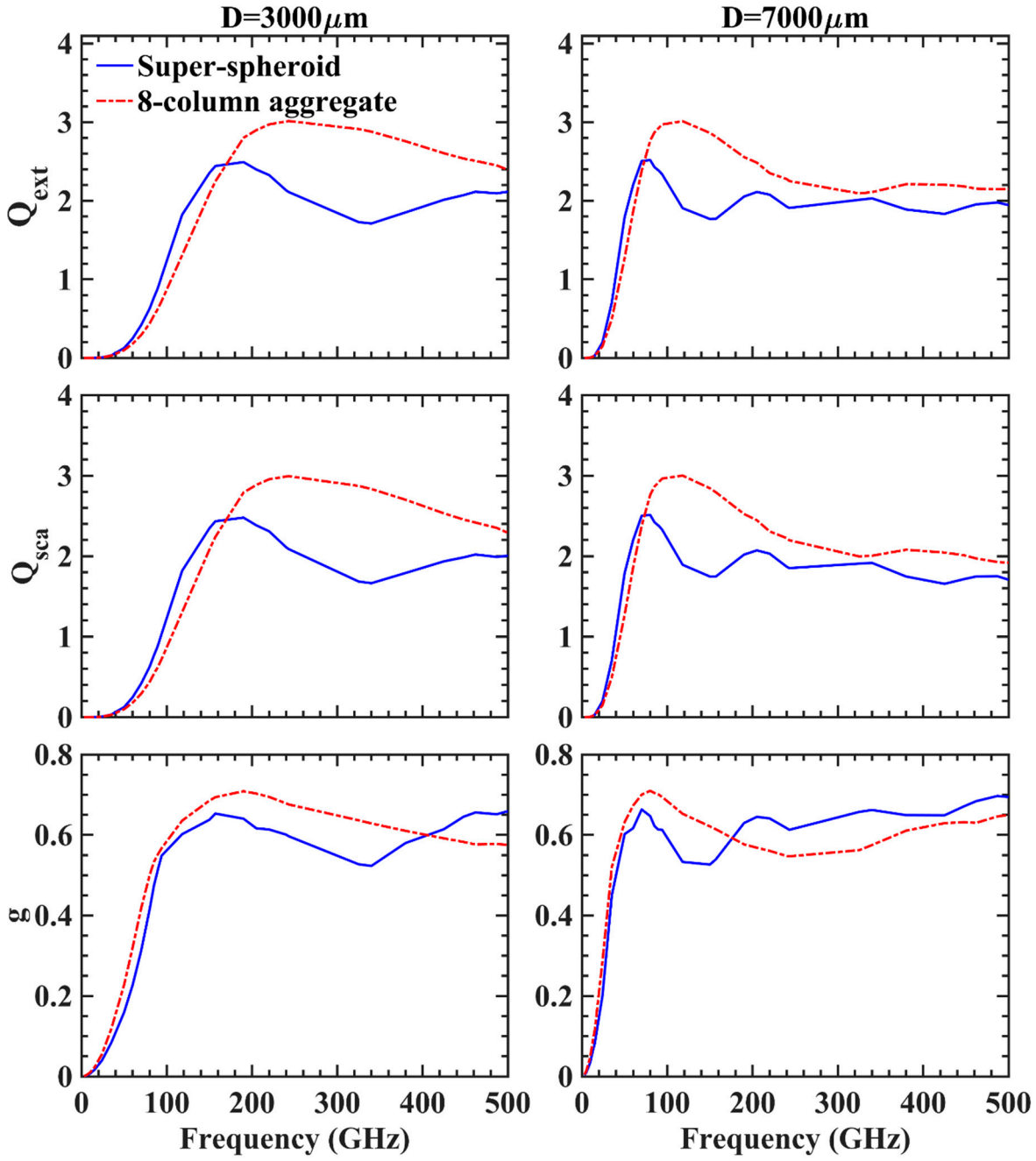

Figure 12. Comparison of the extinction efficiency, scattering efficiency, and asymmetry factor of an 8-column aggregate ice crystal and its corresponding superspheroid in the frequency range of 3–640 GHz. The maximum dimensions of the 8-column aggregate ice crystal were selected as 3000 (**left**) and 7000 (**right**) μm.

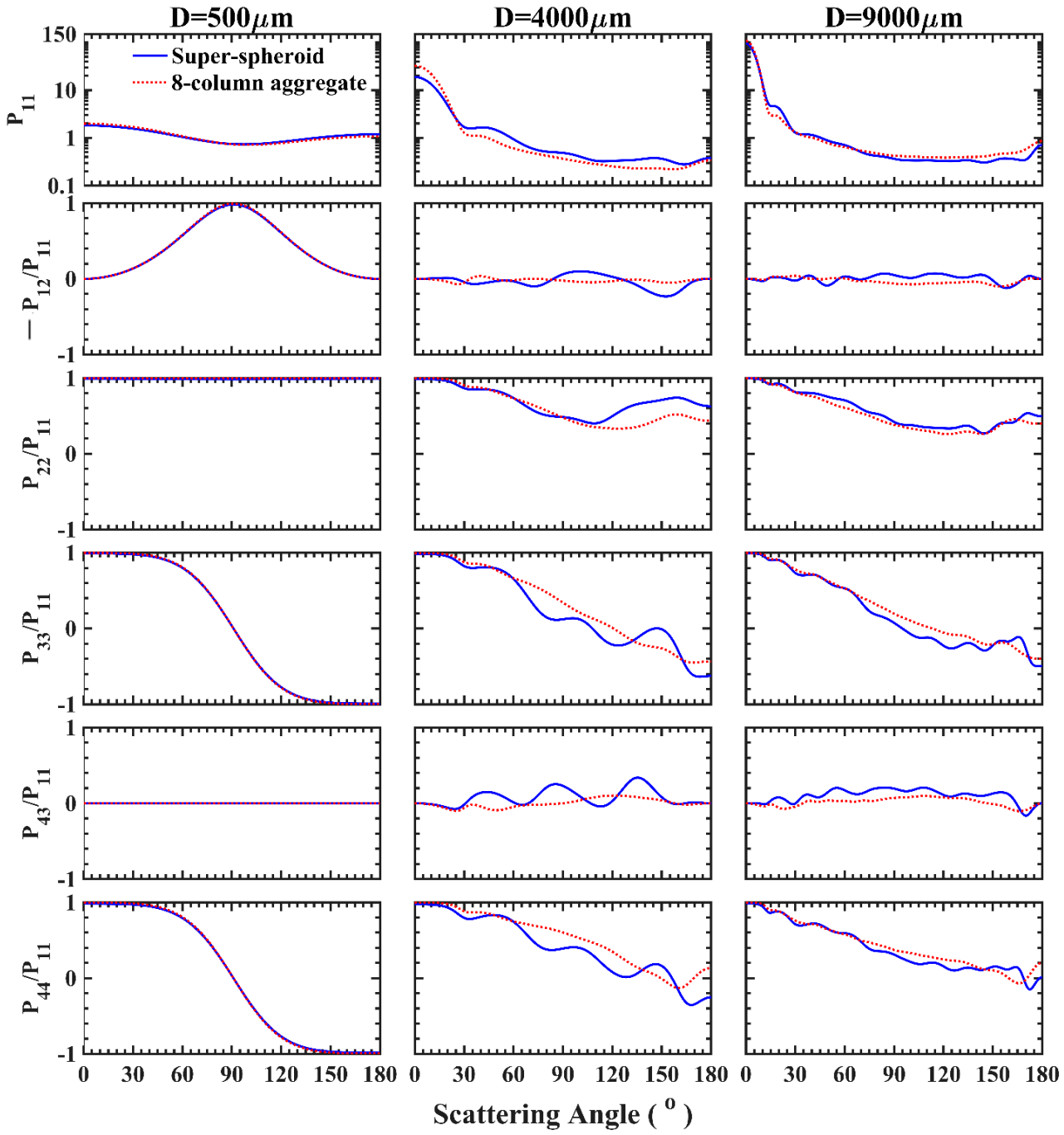

Figure 13. Scattering matrix elements for an 8-column aggregate and superspheroids at the frequency of 220 GHz. The maximum dimensions of the 8-column aggregate ice crystal were selected as 500 (**left**), 4000 (**middle**), and 9000 (**right**) μm.

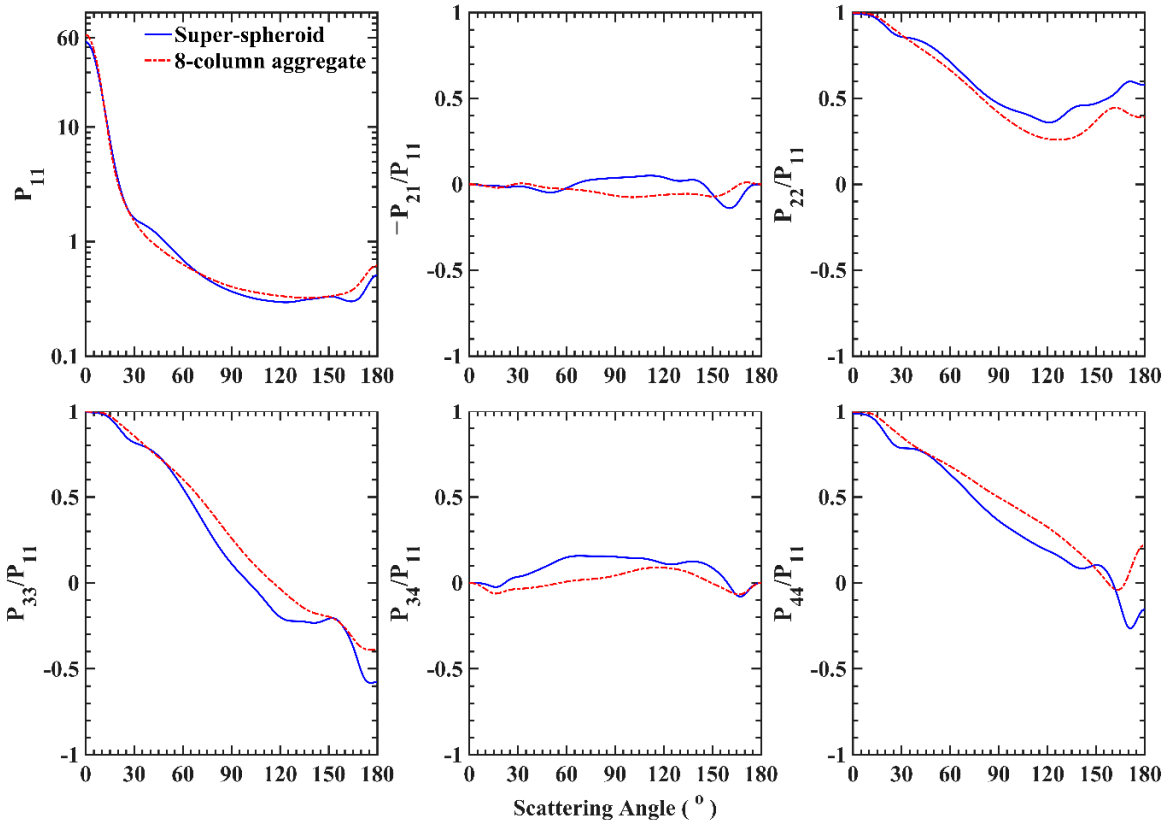

Figure 14. Bulk scattering matrix for an 8-column aggregate and superspheroids. At 220 GHz, the effective diameter (D_m) is 7000 μm, and the effective variance (v_e) is 0.1.

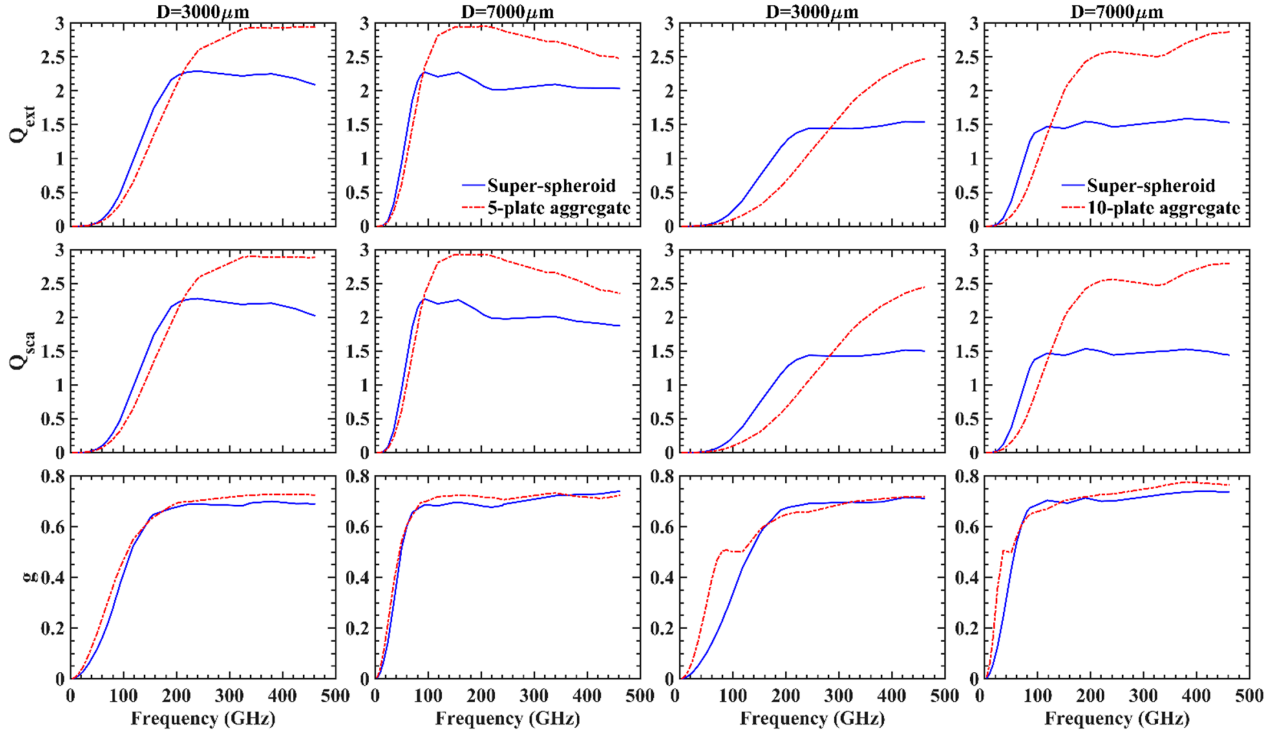

Figure 15. Comparison of the extinction efficiency, scattering efficiency, and asymmetry factor of a plate aggregate ice crystal and its corresponding superspheroid in the frequency range of 3–640 GHz. From left to right: 5-plate aggregate with maximum dimension of 3000 μm, 5-plate aggregate with maximum dimension of 7000 μm, 10-plate aggregate with maximum dimension of 3000 μm, and 10-plate aggregate with maximum dimension of 7000 μm.

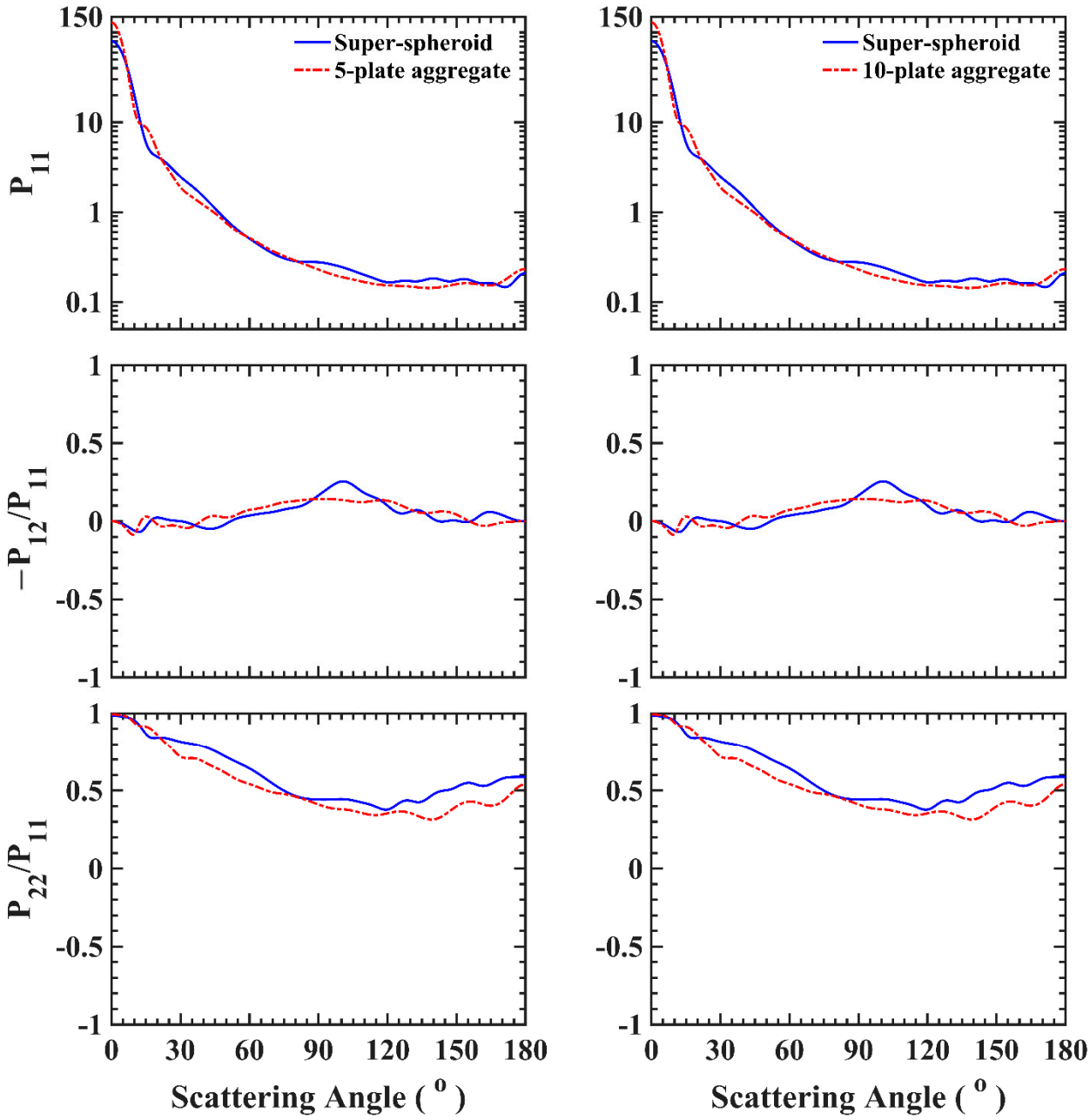

Figure 16. Comparison of phase matrix elements of plate aggregates and their superspheroidal counterparts at the frequency of 220 GHz: 5-plate aggregate (**left**) and 10-plate aggregate (**right**). The maximum dimension D of both 5-plate and 10-plate aggregates is 10,000 μm.

The bulk scattering matrix was computed using the gamma size distribution with D_m of 7000 μm and v_e of 0.1 for the superspheroids and the two aggregate shapes, as shown in Figure 17. Obviously, the oscillation seen in Figure 16 was smoothed after integration. The $-P_{12}/P_{11}$ also had a large difference in the case of 10-plate aggregates. The scattering and extinction coefficients for plate aggregates and their superspheroid counterparts are given in Table 2.

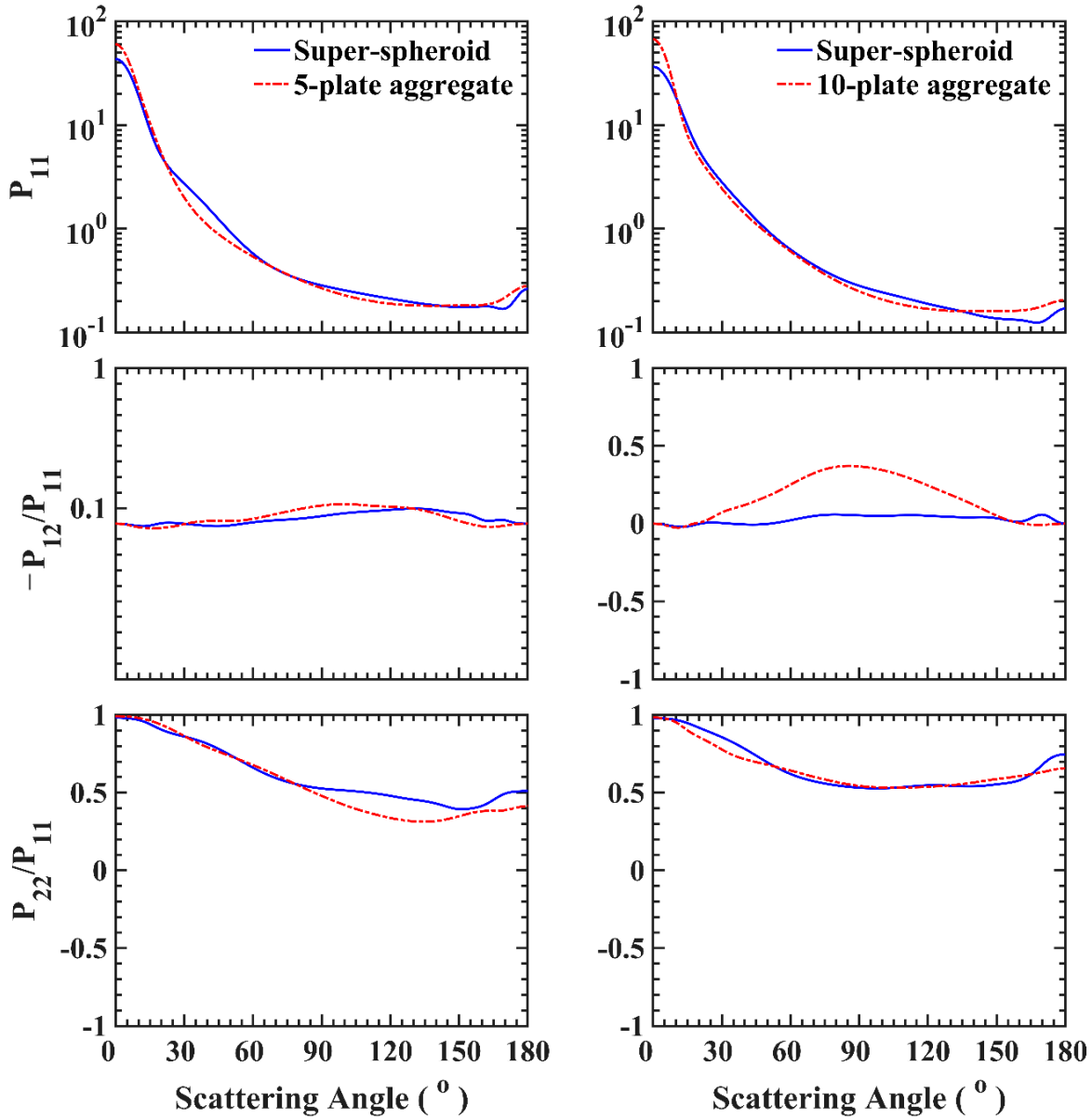

Figure 17. Comparison of bulk scattering matrix elements of plate aggregates and their superspheroidal counterparts at the frequency of 220 GHz: 5-plate aggregate (**left**) and 10-plate aggregate (**right**). In the gamma size distribution, the effective diameter (D_m) is 7000 μm, and the effective variance (v_e) is 0.1.

Note that all the above simulations were in the microwave frequency range. The largest size parameter of all ice crystals was located in the resonant scattering region. In the shortwave regions, the size parameter could be much larger. The shape effect could be pronounced in geometric optics regimes. We will examine the superspheroidal approximation in a few short wavelengths in the next section.

4. Visible and Infrared Wavelengths

We considered three wavelengths (0.66, 2.13, and 11 μm), at which the refractive indices were, $1.3078 + i1.66 \times 10^{-8}$, $1.2677 + i5.255 \times 10^{-4}$, and $1.0086 + i2.478 \times 10^{-1}$, respectively. For each ice crystal model, a total of 45 particle sizes in the range of 2–100 μm were selected. According to the data library from Yang et al. [14], the IITM was used for small size parameters (<~20) and the IGOM (>~20) was used for large size parameters. For the IGOM calculations, three roughness conditions were considered. We followed the surface roughness definition given in [14]; the roughness parameters (σ) were 0, 0.03,

and 0.5, associated with smooth, weakly roughened, and strongly roughened ice crystals, respectively. Note that the calculation of IITM did not consider the surface roughness because the size parameter was relatively smaller.

Figure 18 shows the comparison of phase matrix elements of superspheroid and 8-column aggregate at 0.66 μm. The maximum dimension of the ice particle was chosen as 100 μm. The first column shows the results of the smooth particle (σ = 0). Obviously, the phase function of 8-column aggregate had ice halos at 22 and 46 degrees, which were invisible in the case of superspheroidal particle. The difference is understandable because the superspheroidal particle does not have similar abjoint facets of ice crystals causing the geometric optics halo features. However, as the degree of surface roughness increased, the results of superspheroid and 8-column aggregate were closer. Because the roughened ice crystals have been proven to be more reasonable in developing satellite cloud product, this comparison gives us more confidence in applying the superspheroidal approximation in practical applications. In addition, strong halo peaks in the phase functions stemming from light scattering by smooth ice particles do not appear frequently in reality [27].

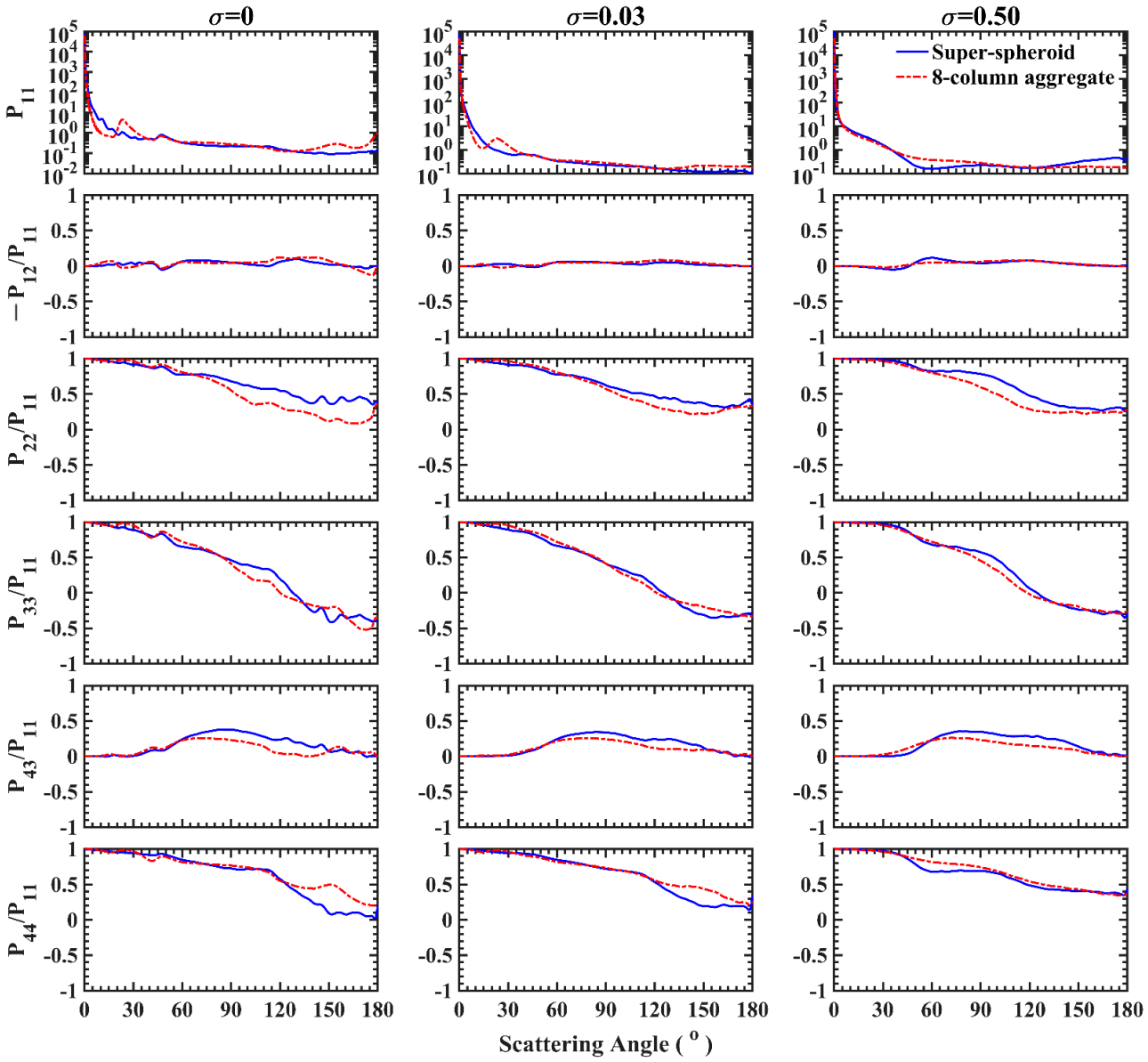

Figure 18. Comparison of scattering matrix elements of three degrees of surface roughness for an 8-column aggregate and its superspheroidal counterparts at the wavelength of 0.66 μm. The maximum dimension (D) of ice crystals is 100 μm.

Figure 19 shows the phase matrix elements for a droxtal (the first column), 8-column aggregate (the second column), and 5-plate aggregate (the third column) at wavelengths of 0.66 μm. We only considered the roughness parameter of 0.5. The results with a maximum dimension of 100 μm were again taken as an example. Figures 20 and 21 are similar to Figure 19 but for the wavelength of 2.13 and 11 μm. It was found that the superspheroids had much better performance in the droxtal case, and the two curves almost coincided. For the 8-column aggregate, the results of P_{11} and $-P_{12}/P_{11}$ at 0.66 and 2.13 μm were better, and the P_{22}/P_{11} at 60–150° were slightly higher than those of the ice crystal model. When the wavelength was 11 μm, the fitting result of the ice crystal model was smoother, but the trend of the two fitting results was similar. For the 5-plate aggregate, the fitting results were better at 0.66 and 2.13 μm, but the P_{44}/P_{11} of superspheroids were slightly lower than that of the ice crystal model, especially for the backscattering (120 to 180°). Note that particles were highly absorptive at 11 μm, but the surface roughness had almost no effect.

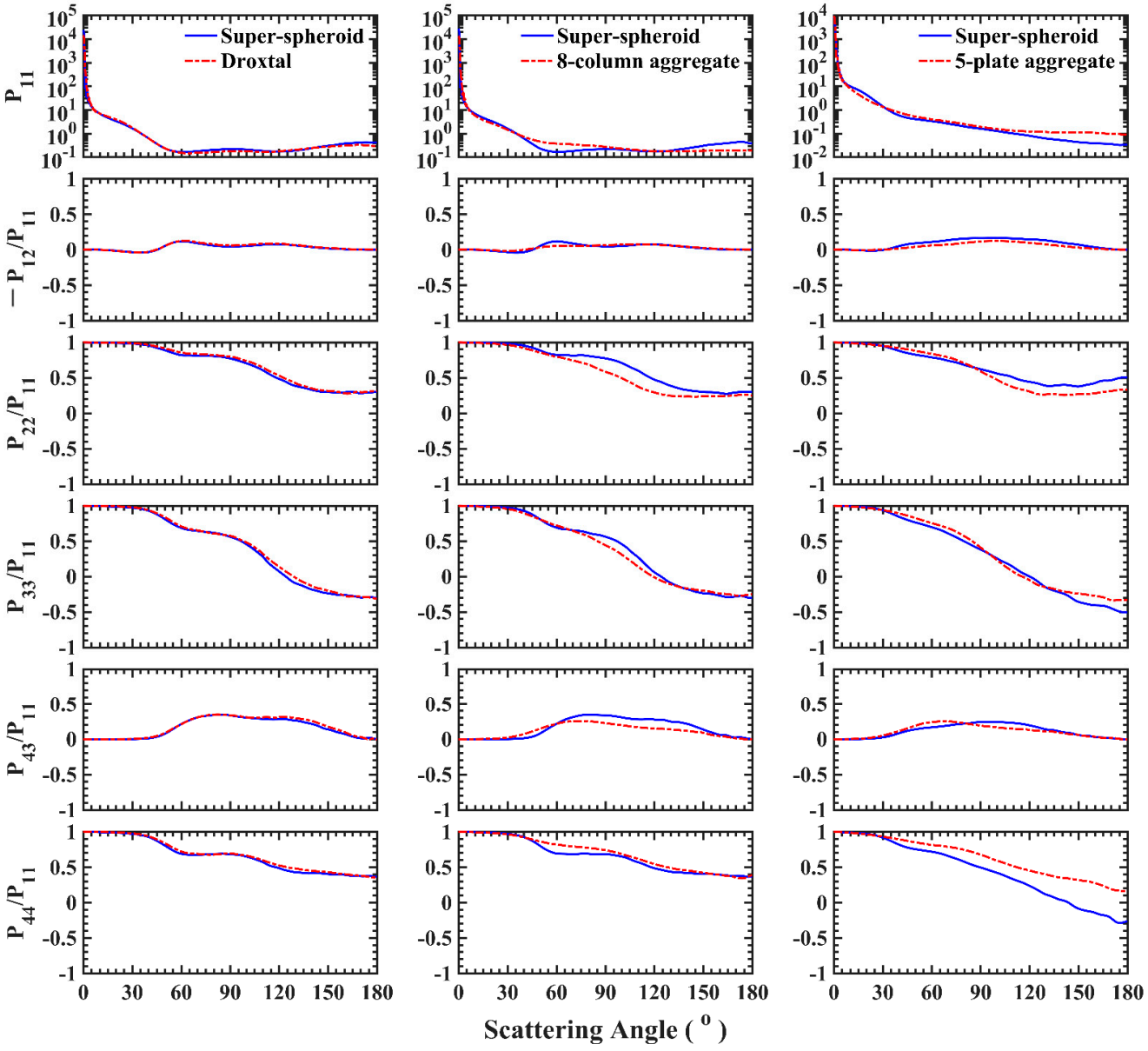

Figure 19. Comparison of scattering matrix elements of three crystal models (droxtal (**left**), 8-column aggregate (**middle**), and 5-plate aggregate (**right**)) and their superspheroidal counterparts at the wavelength of 0.66 μm. The maximum dimension (D) of ice crystals is 100 μm. The degree of surface roughness is 0.5.

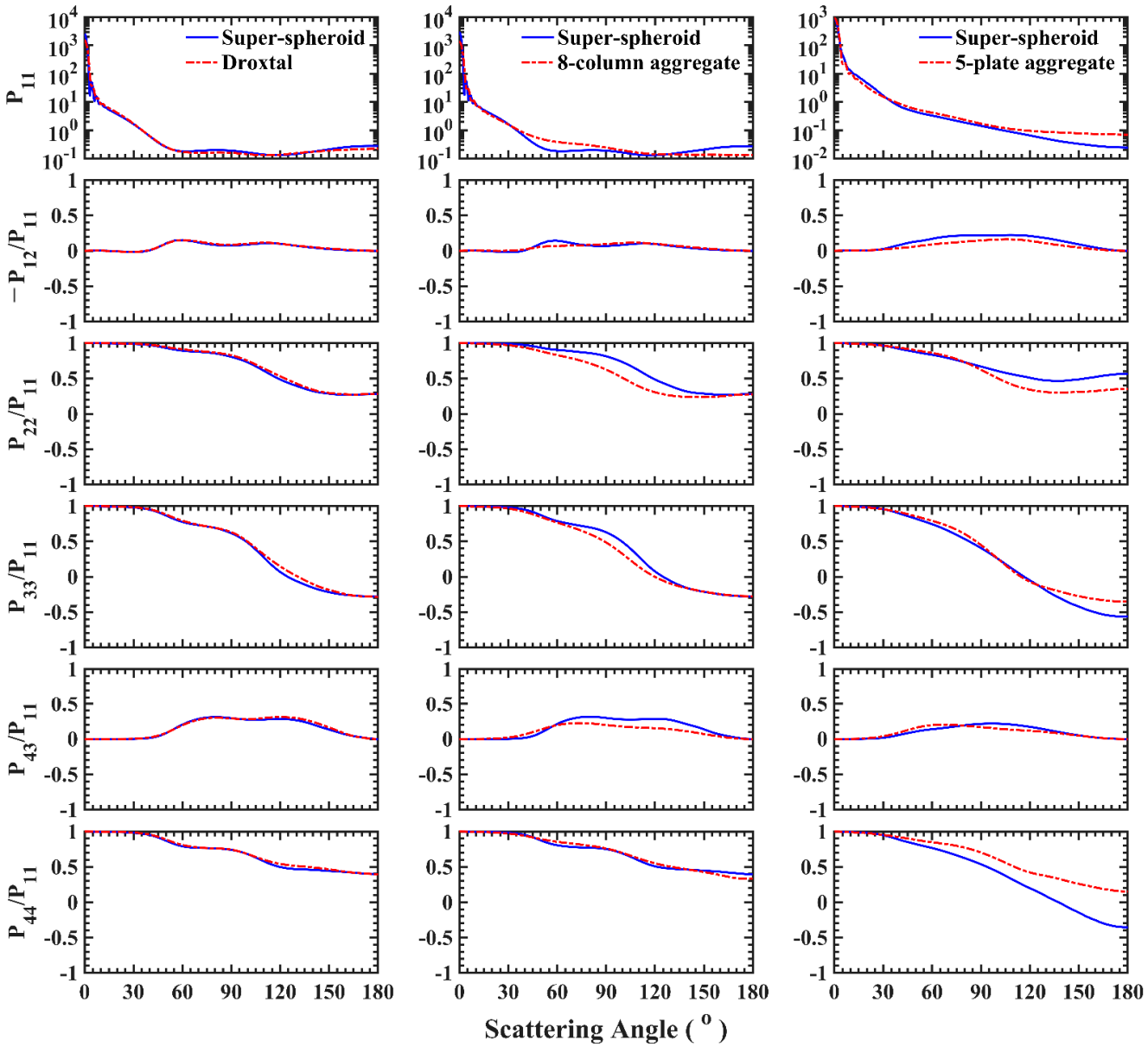

Figure 20. Similar to Figure 19 but for the wavelength of 2.13 μm.

We believe that *SI* and aspect ratio capture essential factors that determine the optical properties. The shape difference of ice crystals and superspheroids could cause additional differences of the optical properties of large particle sizes. However, the condition of surface roughness can inhibit the special morphology effect. Thus, it is expected that better comparison can be made when the surface roughness condition is applied. When the particle is highly absorbing, the diffraction and external reflection dominate the scattering pattern. An observable difference between an ice crystal aggregate and superspheroids is understandable because of distinct multiple external reflections.

The extinction and scattering efficiency factors and asymmetry factor of three shapes are compared in Figures 22–24. Figure 22 shows the IITM results for small-sized smooth particles. This comparison is similar to those in the microwave regions because size parameters are close. The size parameter is defined as kD, where k is the wavenumber. Note that the oscillation of the extinction curve fundamentally stems from the interference between the diffraction and the forward transmission. For a single and compact particle, it is easier to see the oscillation features (see the left droxtal panel). Figure 23 shows the results of large ice crystals computed from the IGOM at the wavelength of 0.66 μm. Two roughness

conditions (0 and 0.5) were considered for comparison. As expected from the previous phase matrix comparisons, the optical similarity between ice crystals and superspheroids was much better for roughened surfaces (the lower three rows) than smooth surfaces (the upper three rows). Figure 24 is similar to Figure 23 but for the wavelength 2.13 μm. Similar conclusions can be obtained from Figures 23 and 24.

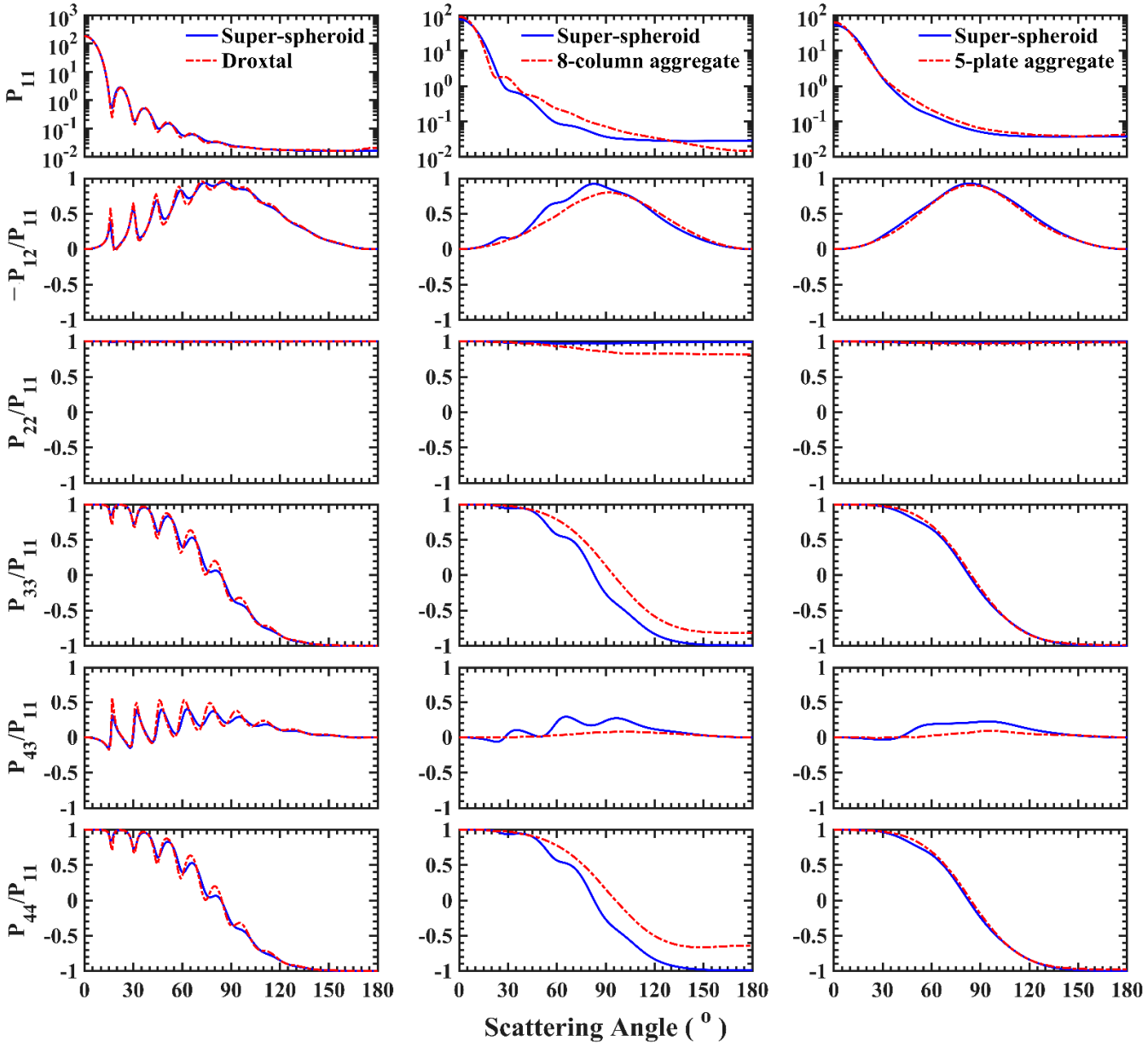

Figure 21. Similar to Figure 19 but for the wavelength of 11 μm.

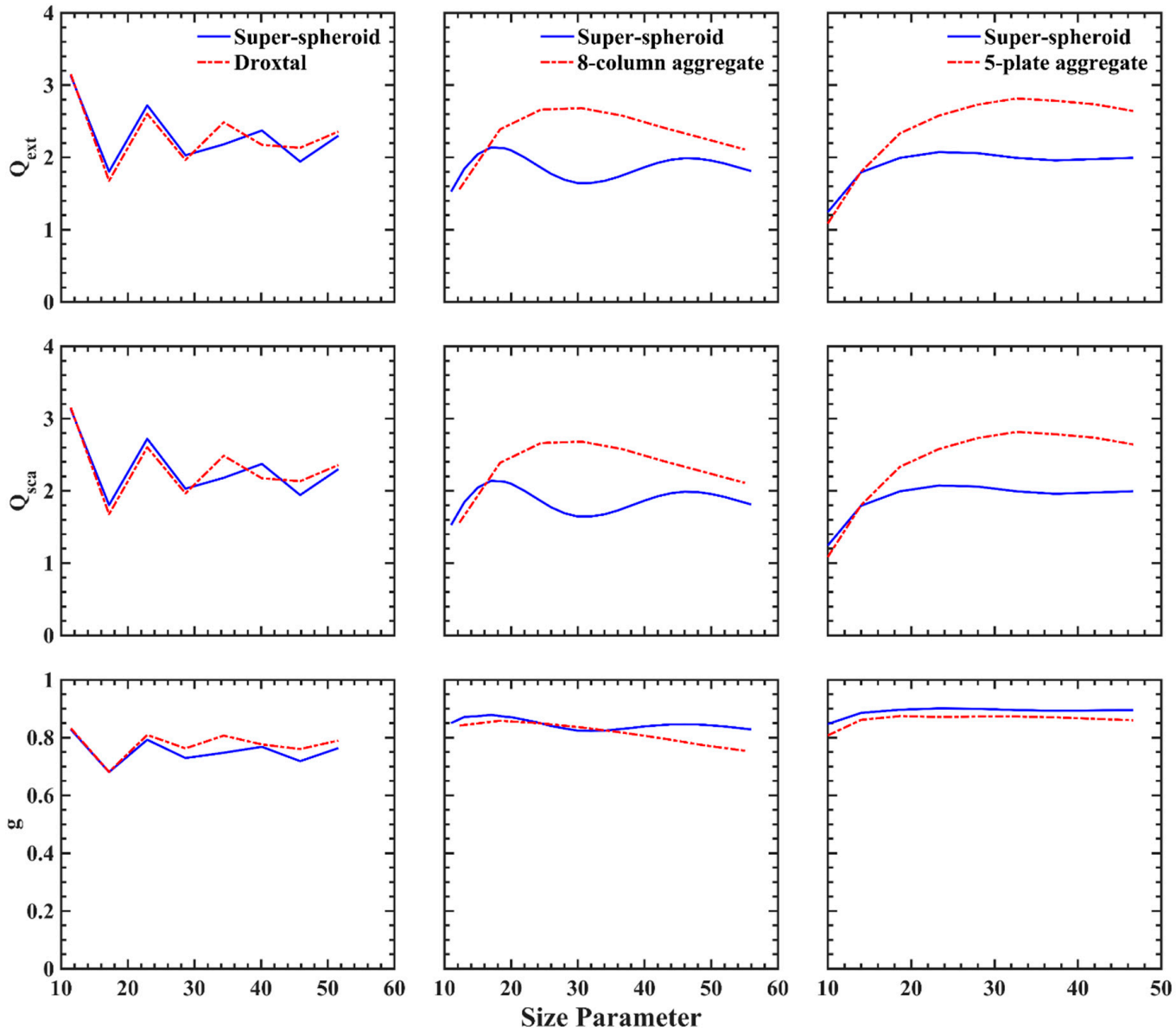

Figure 22. Comparison of the extinction efficiency, scattering efficiency, and asymmetry factor of three ice crystal models (droxtal (**left**), 8-column aggregate (**middle**), and 5-plate aggregate (**right**)) and their superspheroidal counterparts at the wavelength of 0.66 μm. The particle surface is smooth (σ = 0).

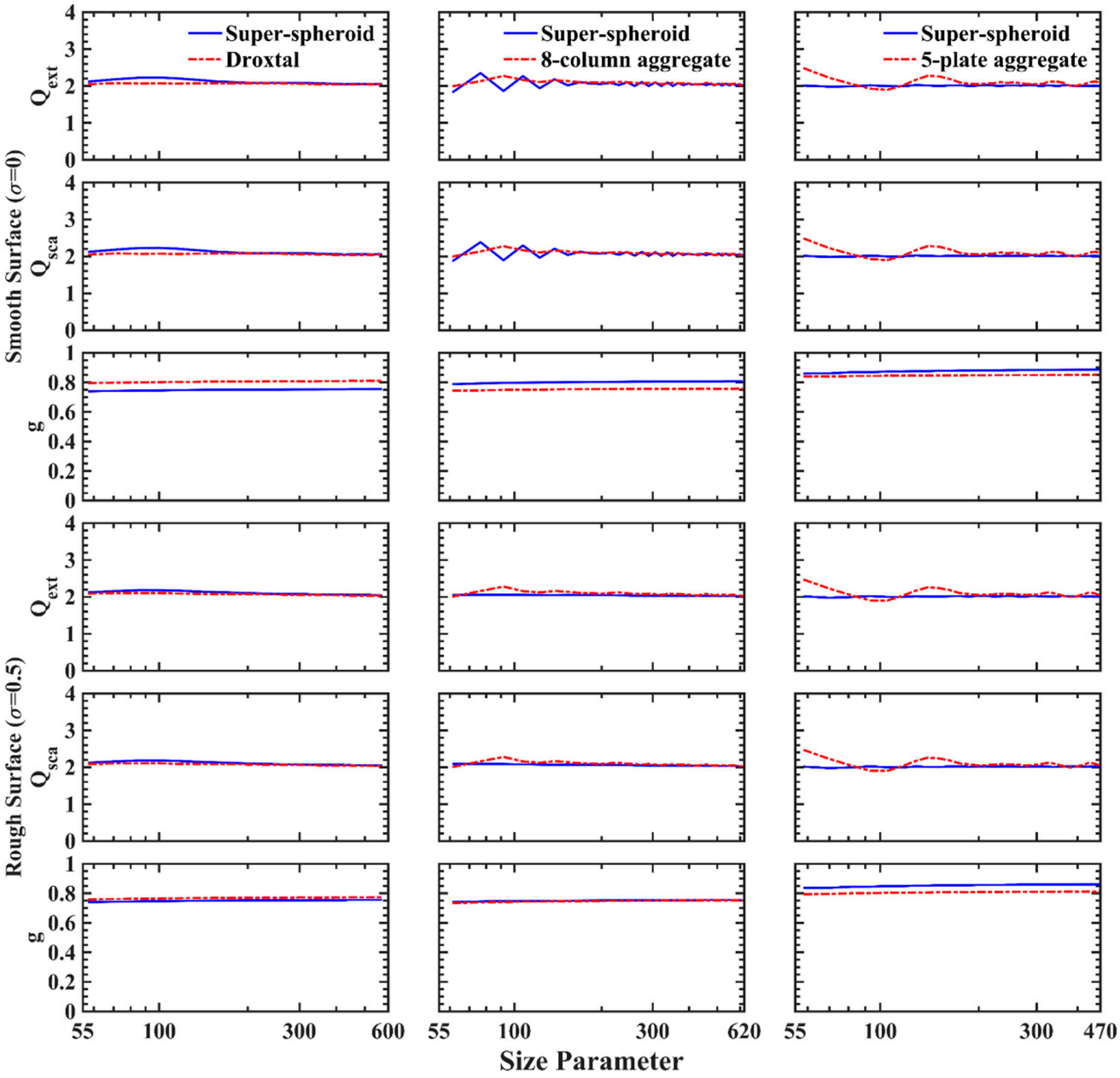

Figure 23. Comparison of the extinction efficiency, scattering efficiency, and asymmetry factor of three ice crystal models (droxtal (**left**), 8-column aggregate (**middle**), and 5-plate aggregate (**right**)) and their superspheroidal counterparts at the wavelength of 0.66 μm. The size parameter is from 55 to 620. For the first three rows, σ = 0, and for the last three rows, σ = 0.5.

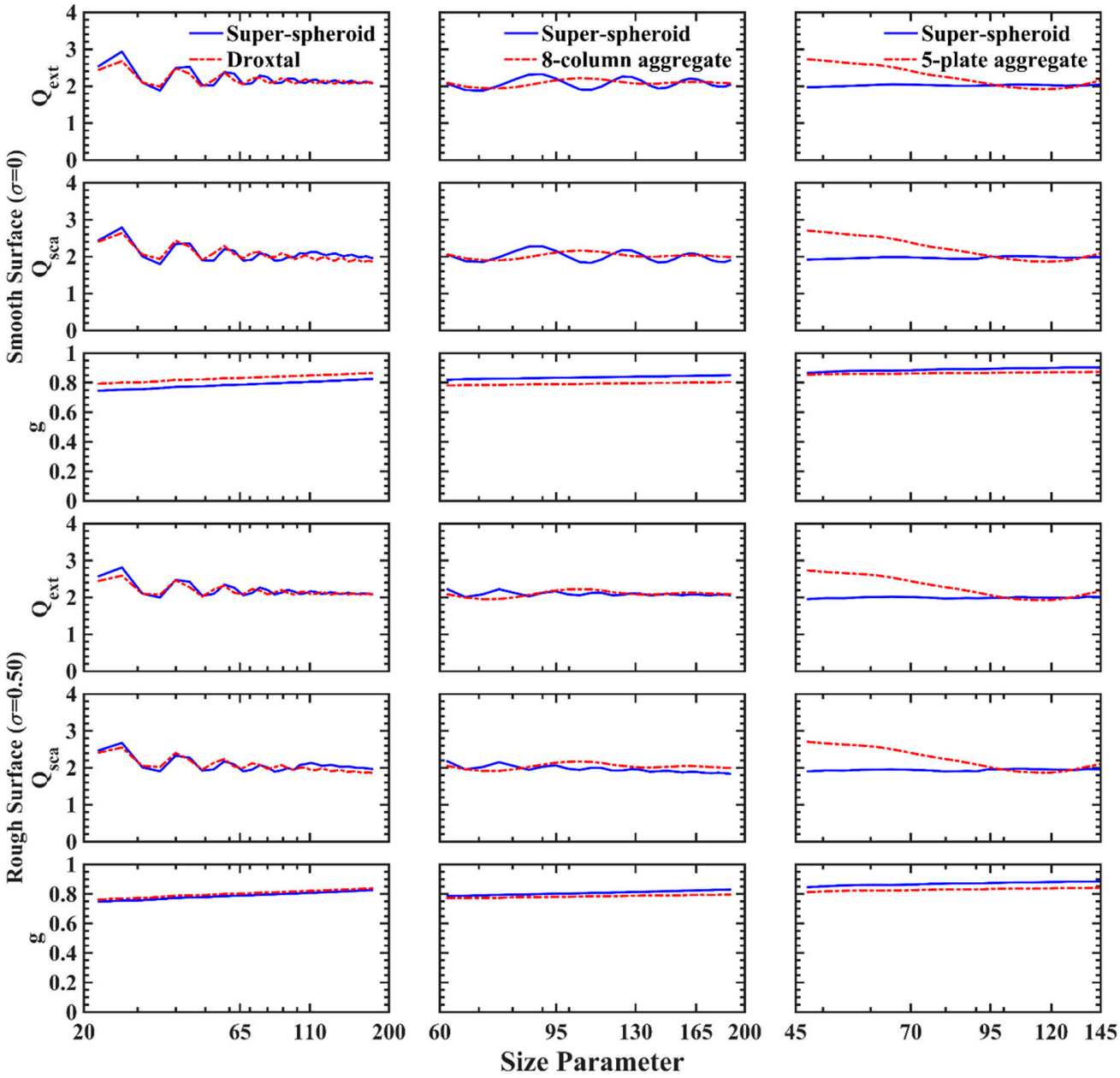

Figure 24. Similar to Figure 23 but for the wavelength of 2.13 μm.

5. Discussions

From the comparisons presented, it is encouraging to find that the single-scattering optical properties of ice crystals can be reasonably reproduced using superspheroidal approximations. Different from the conventional method with the definition of realistic ice crystals shapes, the superspheroid model simplifies the complex nonspherical model by using two parameters: the aspect ratio and the roundness parameter. A continuous change of the shape parameters can be used to construct a shape space with a large range of *SI*s to represent the complexity of realistic ice crystals, which might not be resolved by a few well-defined ice particle shapes. By comparing the scattering efficiency factor, extinction efficiency factor, asymmetry factor, and scattering matrix elements, we confirmed the promising applicability of using superspheroids as surrogates for compact ice crystals. Although for sparse aggregates, the extinction and scattering efficiencies factors in a resonance region could be underestimated, the asymmetry factor and scattering matrix can be approximated with reasonable accuracy.

The aggregation shapes of ice crystals could be much more complex. There may be no aggregate model that can adequately represent realistic ice crystals shapes. In this regard, superspheroidal particles with different *SI*s and aspect rations can be used for sensitivity studies. However, the current approach does not diminish the importance of existing databases based on well-defined ice habits. Databases for canonical ice crystal habits represent the true values for specific habits. Furthermore, it is impossible to use superspheroids for producing particular optical phenomena for smooth ice crystals, such as ice halos, although a higher degree of surface roughness generally results in a smoother phase function.

6. Conclusions

In this paper, superspheroid models are proposed as possible surrogates for representative ice crystal habits to compute the optical properties. The single-scattering properties of ice crystals and superspheroids, including the extinction/scattering efficiency factor, asymmetry factor, and the scattering matrix elements, were systematically compared for representative ice habits, including droxtals, columns, plates, 8-column aggregates, 5-plate aggregates, and 10-plate aggregates. The shape index (*SI*) was found to be quite useful for finding a superspheroid that has high optical similarity to realistic ice crystal shapes.

In both the microwave bands and the visible and the infrared wavelengths, a suitable superspheroid model was identified for each ice crystal, and the single-scattering properties of the superspheroid were close or similar to those of a realistic ice crystal habit.

Given the large range of *SI*s and aspect ratios of superspheroids, the proposed approach is highly promising for modeling the optical properties of ice crystals for atmospheric radiative transfer, remote sensing, and radiative forcing studies. In particular, for realistic ice crystals that cannot be represented by regular ice crystal habits, superspheroids could be used for sensitivity studies and random error estimations. It is believed that a database of superspheroids for ice crystal modeling could provide another valuable alternative for atmospheric scattering and radiative transfer studies.

Superspheroids have already been shown to be powerful for modeling aerosols like dust and sea salt [55,56]. This study indicates that the superspheroidal model may provide a more generalized approach for modeling most atmospheric particles. However, they should not be considered as models that can always perfectly model ice crystals. The performance is expected to worsen as the particle shape becomes sparsely distributed. Thus, some amount of trial and error is unavoidable.

Author Contributions: Conceptualization, L.B. and B.Y.; methodology, L.B.; validation, L.-H.S. and L.B.; formal analysis, L.-H.S. and L.B.; resources, L.B. and B.Y.; data curation, L.-H.S.; writing—original draft preparation, L.-H.S.; writing—review and editing, L.B. and B.Y. All authors have read and agreed to the published version of the manuscript.

Funding: This study was funded by the National Natural Science Foundation of China (42090030, 42022038, 41775130). Bingqi Yi was supported by the Zhujiang Talent Program of the Department of Science and Technology of Guangdong Province (2017GC010619).

Acknowledgments: We acknowledge Rui Liu at the Training Center of Atmospheric Sciences of Zhejiang University for her help with managing computing resources. A portion of the computa-tions was performed at the National Supercomputer Centers in Tianjing (NSCC-TJ), Wuxi(NSCC-WX) and Guangzhou (NSCC-GZ).

Conflicts of Interest: The authors declare no conflict of interest.

References

1. Ramaswamy, V.; Detwiler, A. Interdependence of radiation and microphysics in cirrus clouds. *J. Atmos. Sci.* **1986**, *43*, 2289–2301. [CrossRef]
2. Liou, K.N. Influence of cirrus clouds on weather and climate processes: A global perspective. *Mon. Weather Rev.* **1986**, *114*, 1167–1199. [CrossRef]
3. Baran, A.J. From the single-scattering properties of ice crystals to climate prediction: A way forward. *Atmos. Res.* **2012**, *112*, 45–69. [CrossRef]

4. Baran, A.J. A review of the light scattering properties of cirrus. *J. Quant. Spectrosc. Radiat. Transfer.* **2009**, *110*, 1239–1260. [CrossRef]
5. Yang, P.; Liou, K.N.; Bi, L.; Liu, C.; Yi, B.; Baum, B.A. On the radiative properties of ice clouds: Light scattering, remote sensing, and radiation parameterization. *Adv. Atmos. Sci.* **2015**, *32*, 32–63. [CrossRef]
6. Luo, Z.; Rossow, W.B. Characterizing Tropical Cirrus Life Cycle, Evolution, and Interaction with Upper-Tropospheric Water Vapor Using Lagrangian Trajectory Analysis of Satellite Observations. *J. Clim.* **2004**, *17*, 4541–4563. [CrossRef]
7. Gultepe, I.; Heymsfield, A.J.; Gallagher, M.; Ickes, L.; Baumgardner, D. Ice Fog: The Current State of Knowledge and Future Challenges. Chapter 4, Ice formation and Evolution in Clouds and Precipitation: Measurement and Modelling Challenges. *Meteor. Monogr.* **2017**, *58*, 4.1–4.24. [CrossRef]
8. Heymsfield, A.J.; Miloshevich, L.M. Parameterizations for the Cross-Sectional Area and Extinction of Cirrus and Stratiform Ice Cloud Particles. *J. Atmos. Sci.* **2003**, *60*, 936–956. [CrossRef]
9. Lawson, R.P.; Woods, S.; Jensen, E.; Erfani, E.; Gurganus, C.; Gallagher, M.; Connolly, P.; Whiteway, J.; Baran, A.J.; May, P.; et al. A Review of Ice Particle Shapes in Cirrus formed In Situ and in Anvils. *J. Geophys. Res.* **2019**, *124*, 10049–10090. [CrossRef]
10. Yang, P.; Hioki, S.; Saito, M.; Kuo, C.P.; Baum, B.A.; Liou, K.N. A Review of Ice Cloud Optical Property Models for Passive Satellite Remote Sensing. *Atmosphere* **2018**, *9*, 499. [CrossRef]
11. Gayet, J.F.; Ovarlez, J.; Shcherbakov, V.; Ström, J.; Schumann, U.; Minikin, A.; Auriol, F.; Petzold, A.; Monier, M. Cirrus cloud microphysical and optical properties at southern and northern midlatitudes during the INCA experiment. *J. Geophys. Res.* **2004**, *109*, D20206. [CrossRef]
12. Houghton, J.T.; Hunt, G.E. The detection of ice clouds from remote measurements of their emission in the far-infrared. *Quart. J. Roy. Meteor. Soc.* **1971**, *97*, 1–17. [CrossRef]
13. Baran, A.J.; Hill, P.; Furtado, K.; Field, P.; Manners, J. A Coupled Cloud Physics–Radiation Parameterization of the Bulk Optical Properties of Cirrus and Its Impact on the Met Office Unified Model Global Atmosphere 5.0 Configuration. *J. Clim.* **2014**, *27*, 7725–7752. [CrossRef]
14. Yang, P.; Bi, L.; Baum, B.A.; Liou, K.N.; Kattawar, G.W.; Mishchenko, M.I.; Cole, B. Spectrally Consistent Scattering, Absorption, and Polarization Properties of Atmospheric Ice Crystals at Wavelengths from 0.2 to 100 µm. *J. Atmos. Sci.* **2013**, *70*, 330–347. [CrossRef]
15. Gayet, J.F.; Shcherbakov, V.; Mannstein, H.; Minikin, A.; Schumann, U.; Ström, J.; Petzold, A.; Ovarlez, J.; Immler, F. Microphysical and optical properties of midlatitude cirrus clouds observed in the southern hemisphere during INCA. *Quart. J. Roy. Meteor. Soc.* **2006**, *132*, 2719–2748. [CrossRef]
16. Gultepe, I.; Isaac, G.A.; Joe, P.; Kucera, P.A.; Theriault, J.M.; Fisico, T. Roundhouse (RND) mountain top research site: Measurements and uncertainties for winter alpine weather conditions. *Pure Appl. Geophys.* **2014**, *171*, 59–85. [CrossRef]
17. Gultepe, I. Mountain weather: Observation and modeling. *Adv. Geophys.* **2015**, *56*, 229–312.
18. Liou, K.N. Electromagnetic scattering by arbitrarily oriented ice cylinders. *Appl. Opt.* **1972**, *11*, 667–674. [CrossRef]
19. Liou, K.N. Light scattering by ice clouds in the visible and infrared: A theoretical study. *J. Atmos. Sci.* **1972**, *29*, 524–536. [CrossRef]
20. Stephens, G.L. Radiative properties of cirrus clouds in the infrared region. *J. Atmos. Sci.* **1980**, *37*, 435–446. [CrossRef]
21. Stephens, G.L. Radiative transfer on a linear lattice: Application to anisotropic ice crystal clouds. *J. Atmos. Sci.* **1980**, *37*, 2095–2104. [CrossRef]
22. Liu, L.; Mishchenko, M.I.; Cairns, B.; Carlson, B.E.; Travis, L.D. Modeling single-scattering properties of small cirrus particles by use of a size-shape distribution of ice spheroids and cylinders. *J. Quant. Spectrosc. Radiat. Transfer.* **2006**, *101*, 488–497. [CrossRef]
23. Bohren, C.; Huffman, D. *Absorption and Scattering of Light by Small Particles*; Wiley: New York, NY, USA, 1983.
24. Waterman, P.C. Matrix formulation of electromagnetic scattering. *Proc. IEEE* **1965**, *53*, 805–812. [CrossRef]
25. Mishchenko, M.I.; Travis, L.D. Capabilities and limitations of a current fortran implementation of the T-matrix method for randomly oriented rotationally symmetric scatterers. *J. Quant. Spectrosc. Radiat. Transfer.* **1998**, *60*, 309–324. [CrossRef]
26. Lee, Y.K.; Yang, P.; Mishchenko, M.I.; Baum, B.A.; Hu, Y.X.; Huang, H.L.; Wiscombe, W.J.; Baran, A.J. Use of circular cylinders as surrogates for hexagonal pristine ice crystals in scattering calculations at infrared wavelengths. *Appl. Opt.* **2003**, *42*, 2653–2664. [CrossRef] [PubMed]
27. Mishchenko, M.I.; Macke, A. How big should hexagonal ice crystals be to produce halos? *Appl. Opt.* **1999**, *38*, 1626–1629. [CrossRef]
28. Draine, B.T.; Flatau, P.J. Discrete dipole approximation for scattering calculations. *J. Opt. Soc. Am. A* **1994**, *11*, 1491–1499. [CrossRef]
29. Yurkin, M.A.; Hoekstra, A.G. The discrete-dipole-approximation code ADDA: Capabilities and known limitations. *J. Quant. Spectrosc. Radiat. Transfer.* **2011**, *112*, 2234–2247. [CrossRef]
30. Yee, K. Numerical solution of initial boundary value problems involving Maxwell's equations in isotropic media. *Proc. IEEE* **1966**, *14*, 302–307.
31. Yang, P.; Liou, K.N. Finite-difference time domain method for light scattering by small ice crystals in three-dimensional space. *J. Opt. Soc. Am. A* **1996**, *13*, 2072–2085. [CrossRef]
32. Liu, Q.H. The PSTD algorithm: A time-domain method requiring only two cells per wavelength. *Microw. Opt. Technol. Lett.* **1997**, *15*, 158–165. [CrossRef]

33. Liu, C.; Panetta, R.L.; Yang, P. Application of the pseudo-spectral time domain method to compute particle single-scattering properties for size parameters up to 200. *J. Quant. Spectrosc. Radiat. Transfer.* **2012**, *113*, 1728–1740. [CrossRef]
34. Groth, S.P.; Baran, A.J.; Betcke, T.; Havemann, S.; Śmigaj, W. The boundary element method for light scattering by ice crystals and its implementation in BEM++. *J. Quant. Spectrosc. Radiat. Transfer.* **2015**, *167*, 40–52. [CrossRef]
35. Johnson, B.R. Invariant imbedding T-matrix approach to electromagnetic scattering. *Appl. Opt.* **1988**, *27*, 4861–4873. [CrossRef]
36. Bi, L.; Yang, P. Efficient implementation of the invariant imbedding T-matrix method and the separation of variables method applied to large nonspherical inhomogeneous particles. *J. Quant. Spectrosc. Radiat. Transfer.* **2013**, *116*, 169–183. [CrossRef]
37. Bi, L.; Yang, P.; Kattawar, G.W.; Mishchenko, M.I. A numerical combination of extended boundary condition method and invariant imbedding method to light scattering by large spheroids and cylinders. *J. Quant. Spectrosc. Radiat. Transfer.* **2013**, *123*, 17–22. [CrossRef]
38. Bi, L.; Yang, P. Accurate simulation of the optical properties of atmospheric ice crystals with invariant imbedding T-matrix method. *J. Quant. Spectrosc. Radiat. Transfer.* **2014**, *138*, 17–35. [CrossRef]
39. Takano, Y.; Liou, K.N. Solar radiative transfer in cirrus clouds. Part I: Single-scattering and optical properties of hexagonal ice crystals. *J. Atmos. Sci.* **1989**, *46*, 3–19. [CrossRef]
40. Macke, A.; Mueller, J.; Raschke, E. Single scattering properties of atmospheric ice crystal. *J. Atmos. Sci.* **1996**, *53*, 2813–2825. [CrossRef]
41. Wendling, P.; Wendling, R. Scattering of solar radiation by hexagonal ice crystals. *Appl. Opt.* **1979**, *18*, 2663–2671. [CrossRef] [PubMed]
42. Borovoi, A.G.; Grishin, I.A. Scattering matrices for large ice crystal particles. *J. Opt. Soc. Am. A* **2003**, *20*, 2071–2080. [CrossRef]
43. Muinonen, K. Scattering of light by crystals: A modified Kirchhoff approximation. *Appl. Opt.* **1989**, *28*, 3044–3050. [CrossRef]
44. Yang, P.; Liou, K.N. Geometric-optics-integral- equation method for light scattering by nonspherical ice crystals. *Appl. Opt.* **1996**, *35*, 6568–6584. [CrossRef] [PubMed]
45. Bi, L.; Yang, P.; Kattawar, G.W.; Hu, Y.; Baum, B.A. Scattering and absorption of light by ice particles: Solution by a new physical-geometric optics hybrid method. *J. Quant. Spectrosc. Radiat. Transfer.* **2011**, *112*, 1492–1508. [CrossRef]
46. Masuda, K.; Ishimoto, H.; Mano, Y. Efficient method for computing a geometric optics integral for light scattering. *Meteorol. Geophys.* **2012**, *63*, 15–19. [CrossRef]
47. Hess, M.; Wiegner, M. COP: A data library of optical properties of hexagonal ice crystals. *Appl. Opt.* **1994**, *33*, 7740–7746. [CrossRef]
48. Bi, L.; Yang, P. Improved ice particle optical property simulations in the ultraviolet to far-infrared regime. *J. Quant. Spectrosc. Radiat. Transfer.* **2017**, *189*, 228–237. [CrossRef]
49. Hong, G. Parameterization of scattering and absorption properties of nonspherical ice crystals at microwave frequencies. *J. Geophys. Res.* **2007**, *112*, 11. [CrossRef]
50. Kim, M.J. Single scattering parameters of randomly oriented snow particles at microwave frequencies. *J. Geophys. Res.* **2006**, *111*, D14201. [CrossRef]
51. Liu, G. A Database of Microwave Single-Scattering Properties for Nonspherical Ice Particles. *Bull. Am. Meteorol. Soc.* **2008**, *89*, 1563–1570. [CrossRef]
52. Ding, J.; Bi, L.; Yang, P.; Kattawar, G.W.; Weng, F.; Liu, Q.; Greenwald, T. Single-scattering properties of ice particles in the microwave regime: Temperature effect on the ice refractive index with implications in remote sensing. *J. Quant. Spectrosc. Radiat. Transfer.* **2017**, *190*, 26–37. [CrossRef]
53. Eriksson, P.; Ekelund, R.; Mendrok, J.; Brath, M.; Lemke, O.; Buehler, S.A. A general database of hydrometeor single scattering properties at microwave and sub-millimetre wavelengths. *Earth Syst. Sci. Data* **2018**, *10*, 1301–1326. [CrossRef]
54. Bi, L.; Lin, W.; Liu, D.; Zhang, K. Assessing the depolarization capabilities of nonspherical particles in a super-ellipsoidal shape space. *Opt. Express* **2018**, *26*, 1726–1742. [CrossRef]
55. Lin, W.; Bi, L.; Dubovik, O. Assessing Superspheroids in Modeling the Scattering Matrices of Dust Aerosols. *J. Geophys. Res.* **2018**, *123*, 917–943. [CrossRef]
56. Bi, L.; Lin, W.; Wang, Z.; Tang, X.; Zhang, X.; Yi, B. Optical modeling of sea salt aerosols: The effects of nonsphericity and inhomogeneity. *J. Geophys. Res.* **2018**, *123*, 543–558. [CrossRef]
57. Tang, X.; Bi, L.; Lin, W.; Liu, D.; Zhang, K.; Li, W. Backscattering ratios of soot-contaminated dusts at triple LiDAR wavelengths: T-matrix results. *Opt. Express* **2019**, *27*, A92–A116. [CrossRef]
58. Ishimoto, H.; Masuda, K.; Mano, Y.; Orikasa, N.; Uchiyama, A. Irregularly shaped ice aggregates in optical modeling of convectively generated ice clouds. *J. Quant. Spectrosc. Radiat. Transfer.* **2012**, *113*, 632–634. [CrossRef]
59. Letu, H.; Ishimoto, H.; Riedi, J.; Nakajima, T.Y.; Sekiguchi, M. Investigation of ice particle habits to be used for ice cloud remote sensing for the GCOM-C satellite mission. *Atmos. Chem. Phys.* **2016**, *16*, 12287–12303. [CrossRef]
60. Nousiainen, T.; McFarquhar, G.M. Light scattering by quasi-spherical ice crystals. *J. Atmos. Sci.* **2004**, *61*, 2229–2248. [CrossRef]
61. Barr, A.H. Superquadrics and Angle-Preserving Transformations. *IEEE Comput. Graph. Appl.* **1981**, *1*, 11–23. [CrossRef]
62. Wriedt, T. Using the T-matrix method for light scattering computations by non-axisymmetric particles: Superellipsoids and realistically shaped particles. *Part. Part. Syst. Charact.* **2002**, *19*, 256–268. [CrossRef]
63. Hansen, J.E.; Travis, L.D. Light scattering in planetary atmospheres. *Space Sci. Rev.* **1974**, *16*, 527–610. [CrossRef]

64. Iwabuchi, H.; Yang, P. Temperature dependence of ice optical constants: Implications for simulating the single-scattering properties of cold ice clouds. *J. Quant. Spectrosc. Radiat. Transfer.* **2011**, *112*, 2520–2525. [CrossRef]
65. Yang, P.; Baum, B.A.; Heymsfield, A.J.; Hu, Y.X.; Huang, H.L.; Tsay, S.C.; Ackerman, S. Single-scattering properties of droxtals. *J. Quant. Spectrosc. Radiat. Transfer.* **2003**, *79–80*, 1159–1169. [CrossRef]
66. Auer Jr, A.H.; Veal, D.L. The dimension of ice crystals in natural clouds. *J. Atmos. Sci.* **1970**, *27*, 919–926. [CrossRef]
67. Mitchell, D.L.; Arnott, W.P. A model predicting the evolution of ice particle size spectra and radiative properties of cirrus clouds. Part II: Dependence of absorption and extinction on ice crystal morphology. *J. Atmos. Sci.* **1994**, *51*, 817–832. [CrossRef]
68. Pruppacher, H.; Klett, J. *Microphysics of Clouds and Precipitation*; Springer: Berlin/Heidelberg, Germany, 1980.
69. Platnick, S.; Meyer, K.G.; King, M.D.; Wind, G.; Amarasinghe, N.; Marchant, B.; Arnold, G.T.; Zhang, Z.; Hubanks, P.A.; Holz, R.E.; et al. The MODIS cloud optical and microphysical products: Collection 6 updates and examples from Terra and Acqua. *IEEE Trans. Geosci. Remote Sens.* **2016**, *55*, 502–525. [CrossRef]
70. Fox, S. An Evaluation of Radiative Transfer Simulations of Cloudy Scenes from a Numerical Weather Prediction Model at Sub-Millimetre Frequencies Using Airborne Observations. *Remote Sens.* **2020**, *12*, 2758. [CrossRef]